Multicomponent states for trapped spin-1 Bose-Einstein condensates in the presence of a magnetic field

Projjwal K. Kanjilal [*] and A. Bhattacharyay [†]
Department of Physics, Indian Institute of Science Education and Research, Dr. Homi Bhabha Road, Pune 411 008, India

(Received 18 February 2023; revised 5 July 2023; accepted 30 October 2023; published 27 November 2023)

In the presence of a magnetic field, multicomponent ground states appear in trapped spin-1 Bose-Einstein condensates for both ferromagnetic and antiferromagnetic types of spin-spin interaction. We aim to produce an accurate analytical description of the multicomponent states which is of fundamental importance. Despite being in the so-called regime of the Thomas-Fermi approximation (condensates with large particle number), the scenario of multicomponent states is problematic under this approximation due to the large variation in densities of the subcomponents. We generalize the variational method that we have introduced [P. K. Kanjilal and A. Bhattacharyay, Eur. Phys. J. Plus **137**, 547 (2022)] to overcome the limitations of the Thomas-Fermi approximation. We demonstrate that the variational method is crucial in identifying multicomponent ground states. A comparison of the results of the variational method, which is multimodal by construction, with that of the single-mode approximation is also presented in this paper to demonstrate a marked improvement in accuracy over the single-mode approximation. We have also looked into the phase transition between phase-matched and polar states in a trapped condensate using the variational method and have identified substantial change in the phase boundary. The correspondence of the phase diagram of the trapped case with the homogeneous one identifies other limitations of the Thomas-Fermi approximation as opposed to the more accurate variational method.

DOI: 10.1103/PhysRevA.108.053322

I. INTRODUCTION

The successful experimental realization of Bose-Einstein condensates (BECs) with alkali-metal atoms [1–3] inside a magnetic trap spurred renewed interest [4–6] in ultracold atomic physics. Soon it attracted a lot of attention from both atomic and condensed-matter physics communities as it provided an ideal test bed as a quantum simulator [7–12] and precision measurements [13–18] for its unprecedented experimental control.

Early experiments on BECs [19,20] were done in a magnetic trap, which only captures atoms with weak-field-seeking hyperfine states; thus, the magnetic degrees of freedom were frozen in the resulting BEC. Later, with the optical trapping technique, this limitation was overcome, and spinor BECs were created with all the hyperfine states of the constituent spin-f atoms (f is an integer) [21–23]. The order parameter of such a system has $(2f + 1)$ components. Due to the interplay of magnetic field and interatomic interaction, the spinor BEC shows a rich variety of phenomena, including spin textures [24,25], domain structures [26–45], and topological phases [46]. Spinor BECs also attracted a lot of attention due to their complex soliton structures [47–50], interesting few-body physics in low dimensions [51].

The role of accurately known density profiles of the multicomponent ground state is crucial in dealing with a plethora of interesting phenomena that occur in spinor BECs. As a result, there have been a lot of studies on multicomponent ground states [52–55]. But, most of those analytical studies are based on the Thomas-Fermi (TF) approximation and single-mode approximation (SMA) for the sake of simplicity. However, there exists scope for a wrong interpretation of the ground-state structure of multicomponent BECs under the TF approximation and similarly wrong estimation of ground-state density profiles under the SMA which could lead to problems in the presence of closely competing candidate states.

Both of these problems could be overcome by the method of variational analysis [56] of the ground-state profile in a multimodal manner. One can accurately identify the structure of the tail of density profiles using low-lying oscillator states in a harmonic trap along with the correction to the subcomponent density in the central region of the trap. In the present paper, we identify the problems with the TF approximation and SMA interpretations and compare the results of these methods vis-à-vis the more accurate variational method [56] extended to work for a wide range of magnetic field conditions.

In this paper, we look at confined spin-1 BECs in the presence of the magnetic field in the absence of any finite-temperature [57–59] or interparticle correlation effects [60]. To get to the ground state, one has to solve the Gross-Pitaevskii (GP) equations which govern the dynamics of the three-component order parameter (the mean fields ψ_1, ψ_0, and ψ_{-1}). In the absence of trapping, solving the GP equations, one can get to the phase diagram in p, q parameter space [23,61,62], where p and q are the linear and quadratic Zeeman terms, respectively, that capture the contribution coming from the magnetic field.

We first consider quasi-one-dimensional ^{87}Rb and ^{23}Na systems under harmonic trapping. For the ^{87}Rb, the TF

[*] projjwal.kanjilal@students.iiserpune.ac.in
[†] a.bhattacharyay@iiserpune.ac.in

approximation predicts a domainlike structure between the phase-matched (PM) state near the center of the trap followed by the polar state outside. Similarly, for a specific choice of Zeeman terms, the TF approximation predicts the ground state to be a domain structure between the antiferromagnetic and ferromagnetic states in ^{23}Na. For multicomponent states in the presence of the magnetic field, i.e., for a nonzero contribution of the linear and quadratic terms, no matter how large the number of particles present in the condensate may be, the TF approximation indicates the domain structure in the ground state, which numerical results do not validate. Using the generalized multimodal variational method, we establish that there is no domain structure in the ground states of the above-mentioned cases. The multicomponent stationary state at the core of the trap is the ground state in all the cases.

We also take into account the results of the SMA, which is widely used to capture the physics of spin-oscillation dynamics [53,62–65], for a comparison with those of our variational method. We look into an experimentally relevant case where the contribution coming from the linear Zeeman term is bypassed by moving to a rotating frame to effectively set $p = 0$ [66]. This is a standard procedure for the application of the SMA. However, the SMA does not provide a good estimation of the subcomponent density profiles for the ground state of the ^{87}Rb condensate particularly having large deviations from numerical results across the whole density range. Our multimodal variational method works quite accurately in comparison to the SMA to account for the ground-state density profiles. This further emphasizes the merit of the variational method to analytically capture the multimodal nature of states.

Having shown these results for a quasi-one-dimensional trap that standardizes the variational method to its multimodal form, in this paper we embark on identifying the phase boundary between the PM and the polar state for a three-dimensional condensate in isotropic harmonic trapping. The phase diagram between the PM and the polar state is known in the homogeneous (untrapped) case. From the variational method, we show that there arises a significant shift in the phase boundary in the trapped case, which the numerical results also verify. However, the phase boundaries for different particle numbers in the trapped case could be collapsed to manifest the correspondence between the trapped and homogeneous systems. The single parameter, dependent on the number of particles in the trapped condensate, that scales the phase boundaries is the value q_t^{tr} of q' at $p' = 0$, where the phase transition happens (p' and q' are in dimensionless representation, which we introduce later). This parameter comes out to scale with the particle number as $q_t^{tr} \sim N^{3/4}$. An equivalent parameter from the mapping of the TF approximated trapped condensate to its homogeneous equivalent results in $q_t^{\mathrm{TF}} \sim N^{2/5}$. This presents a clear distinction of the results of the variational method in comparison to the TF approximation which could be probed by experiments.

For a condensate with the ferromagnetic type of spin-spin interaction initially in a ground state that corresponds to the polar state, if the magnetic field is rapidly quenched to a smaller q for a constant p, across the phase boundary, the ground state is supposed to change to that of the PM state, i.e., the broken-axisymmetry phase [62]. This sudden quench in the magnetic field (quench in q at $p = 0$; see Sec. 5.9 of Ref. [62]) across the phase transition boundary between the PM state and the polar state is of high importance in the context of the Kibble-Zurek mechanism and the associated creation of spin vortices [67–69]. Thus, an accurate estimation of the phase boundary of the PM state and the polar state for a trapped condensate, shown in this article, is of high relevance from an experimental point of view as well.

The article is organized in the following way. In Sec. II, we discuss the mean-field theory of the spin-1 trapped BEC in the presence of the magnetic field. In Sec. III we focus on the analytical description of the phase-matched state and the antiferromagnetic state that become ground states for ^{87}Rb and ^{23}Na, respectively. We start with the TF approximated results and then we provide a description based on the variational method and compare it with the numerical simulation. We compare the results of the SMA with those of the variational method to demonstrate the improvement offered by the latter. Following this, in Sec. IV, we estimate the phase boundary between the PM state and the polar state for a similar condensate in an isotropic three-dimensional harmonic trap to explore the correspondence to the homogeneous case. This is followed by a discussion on the generality of the treatment presented here and possible directions to explore.

II. MEAN-FIELD THEORY: GP EQUATION

The dynamics of the mean fields for a trapped spin-1 BEC in the presence of a magnetic field is captured in the GP equation [45,52,62,70],

$$i\hbar\frac{\partial\psi_m}{\partial t} = \left(-\frac{\hbar^2\nabla^2}{2M} + U(\vec{r}) - pm + qm^2 + c_0 n\right)\psi_m + c_1\sum_{m'=-1}^{1}\vec{F}\cdot\vec{f}_{mm'}\psi_{m'}, \tag{1}$$

where the first term on the right is the kinetic energy contribution for particles of mass M. The second term is due to the confining potential and the presence of the magnetic field is captured by the linear and quadratic Zeeman terms p and q, respectively. We assume a two-body contact interaction that can be decomposed into spin-independent (the term involving c_0) and interspin interactions (the term with c_1). As this is a spin-1 system, the subscripts m and m' take the values 1, 0, and -1.

The total density n is defined as

$$n(r) = \sum_{m=-1}^{1}|\psi_m|^2, \tag{2}$$

and the local spin density $\vec{F}$ is

$$\vec{F} = \sum_{i,j=-1}^{1}\psi_i^*\vec{f}_{ij}\psi_j, \tag{3}$$

where the $\vec{f}$ is defined via the spin-1 Pauli matrices [62]. The GP equation [Eq. (1)] is a set of three coupled nonlinear partial differential equations that yields the order parameter $(\psi_1, \psi_0, \psi_{-1})$ as its solution.

The mean-field approximated total energy [62],

$$E = \int d\vec{r} \sum_{m=-1}^{1} \psi_m^* \left(-\frac{\hbar^2 \nabla^2}{2M} + U(\vec{r}) - pm + qm^2 \right) \psi_m + \frac{c_0}{2} n^2 + \frac{c_1}{2} |\vec{F}|^2, \tag{4}$$

can be compared for different stationary states to get to the ground state of the system. In this paper, we represent the stationary states as $(\mathbb{n}_1, \mathbb{n}_0, \mathbb{n}_{-1})$, where $\mathbb{n}_m$ is the placeholder for the binary notation, 0 or 1. If the subcomponents are populated we represent it as 1 and if empty we represent it as 0. In this notation, for example, the ferromagnetic state is represented as (1,0,0) or (0,0,1), where the subcomponent corresponding to $m = 1$ or $m = -1$ is populated.

To simplify the GP equations further, one can write the mean fields in terms of the density and corresponding phase,

$$\psi_m(\vec{r}, t) = \sqrt{n_m(\vec{r})} \exp\left(-\frac{i\mu t}{\hbar} \right) \exp(-i\theta_m), \tag{5}$$

where the parameter μ stands for the chemical potential. One can get the number and phase dynamics separately [45] by using this ansatz in Eq. (1),

$$\dot{n}_0(\vec{r}) = -\frac{4c_1 n_0 \sqrt{n_1 n_{-1}} \sin\theta_r}{\hbar}, \tag{6}$$

$$\dot{n}_{\pm 1}(\vec{r}) = \frac{2c_1 n_0 \sqrt{n_1 n_{-1}} \sin\theta_r}{\hbar}, \tag{7}$$

$$\hbar\dot{\theta}_0 = \frac{1}{\sqrt{n_0(\vec{r})}} (\mathcal{H} - \mu) \sqrt{n_0(\vec{r})} + c_1 (n_1 + n_{-1} + 2\sqrt{n_{-1} n_1} \cos\theta_r), \tag{8}$$

$$\hbar\dot{\theta}_{\pm 1} = \frac{1}{\sqrt{n_{\pm 1}(\vec{r})}} (\mathcal{H} - \mu) \sqrt{n_{\pm 1}(\vec{r})} \pm c_1 (n_1 - n_{-1}) + q \mp p + c_1 n_0 \left(1 + \sqrt{\frac{n_{\mp 1}(\vec{r})}{n_{\pm 1}(\vec{r})}} \cos\theta_r \right), \tag{9}$$

where $\mathcal{H} = -\frac{\hbar^2 \nabla^2}{2M} + U(\vec{r}) + c_0 n$ and θ_r is the relative phase which is defined as $\theta_r = \theta_1 + \theta_{-1} - 2\theta_0$ [62]. The same ansatz [Eq. (5)] makes the energy a function of the subcomponent number density and the relative phase,

$$\begin{aligned} E &= \int d\vec{r} e(\vec{r}) \\ &= \int d\vec{r} \left(-\sum_{m=-1}^{1} \sqrt{n_m(\vec{r})} \frac{\hbar^2 \nabla^2}{2M} \sqrt{n_m(\vec{r})} \right. \\ &\quad + U(\vec{r}) n(\vec{r}) - p(n_1 - n_{-1}) + q(n_1 + n_{-1}) \\ &\quad + \frac{c_0}{2} n^2(\vec{r}) + \frac{c_1}{2} (n_1 - n_{-1})^2 \\ &\quad \left. + c_1 n_0 [n_1 + n_{-1} + 2\sqrt{n_1 n_{-1}} \cos\theta_r] \right), \end{aligned} \tag{10}$$

where $e(\vec{r})$ is the energy density. Note that, in this article, we are not looking for vortex solutions. Thus, in Eqs. (6)–(10) we have neglected the spatial variation of the subcomponent phases, assuming that the phases are either constant or varying slowly.

For the stationary states, there is no temporal variation of the subcomponent number densities and the subcomponent phases; i.e., the left-hand sides of Eqs. (6)–(9) can be equated to zero. From Eqs. (6) and (7), one can conclude that at least one of the subcomponents should be empty to satisfy the equations. Otherwise, the relative phase has to be either zero or π when all the subcomponents are populated. Such a stationary state is also known as the phase-matched (PM) state for $\theta_r = 0$ and the anti-phase-matched (APM) state for $\theta_r = \pi$. The subcomponent phase equations [Eqs. (8) and (9)] for a particular stationary state can be solved to get the subcomponent number densities and, therefore, the total energy. Before going into that, we will rewrite these equations in a nondimensional form.

We consider the system to be in quasi-one-dimensional harmonic confinement; i.e., the condensate is elongated along the x axis. This means the trapping frequency along the x direction is much less than the geometric mean of the trapping frequencies along the other two directions; i.e., $\omega_x \ll \omega_{yz}$, where $\omega_{yz} = \sqrt{\omega_y \omega_z}$. The number density and the interaction parameters are scaled as [56]

$$c_0 = 2\pi l_{yz}^2 l_x \lambda_0 \hbar \omega_x, \quad c_1 = 2\pi l_{yz}^2 l_x \lambda_1 \hbar \omega_x, \tag{11}$$

$$u_m = 2\pi l_{yz}^2 l_x n_m, \quad r = l_x \zeta, \tag{12}$$

where $l_x^2 = \hbar/(m\omega_x)$, $l_{yz}^2 = \hbar/(m\omega_{yz})$, and N is the total number of particles in the condensate. As a result, the parameters λ_0, λ_1, ζ, and u_m become all dimensionless.

The phase equations can now be written as [imposing the stationarity condition in Eqs. (8) and (9)]

$$\left\{ -\frac{1}{2}\frac{d^2}{d\zeta^2} + \frac{1}{2}\zeta^2 + \lambda_0 u - \mu' + \lambda_1 (u_1 + u_{-1} + 2\sqrt{u_{-1} u_1} \cos\theta_r) \right\} \sqrt{u_0} = 0, \tag{13}$$

$$\left\{ -\frac{1}{2}\frac{d^2}{d\zeta^2} + \frac{1}{2}\zeta^2 + \lambda_0 u - \mu' \pm \lambda_1 (u_1 - u_{-1}) \mp p' + q' \right\} \times \sqrt{u_{\pm 1}} + \lambda_1 u_0 (\sqrt{u_{\pm 1}} + \sqrt{u_{\mp 1}} \cos\theta_r) = 0, \tag{14}$$

where, μ', p', and q' correspond to the dimensionless forms of chemical potential, and the linear and quadratic Zeeman terms, respectively. The scaling is done by dividing the parameters with the factor $\hbar\omega_x$. The subcomponent densities add up to provide the total density of the system; i.e., $u = u_1 + u_0 + u_{-1}$.

If the kinetic energy contribution is negligible in comparison to the interaction terms, then one can use the TF approximation and solve Eqs. (13) and (14) to get the subcomponent number densities and, hence, the energy density or the total energy for different stationary states. The TF-approximated results of ground states of our present interest are detailed in Table I.

III. MULTICOMPONENT STATIONARY STATES

Consider a quasi-one-dimensional cigar-shaped harmonic confinement of trapping frequency along the elongated

TABLE I. The density and the energy density expressions corresponding to different stationary states at $\lambda_1 \neq 0$ obtained via TF approximation [45]. All the parameters in this table are in dimensionless form. One can use Eqs. (11) and (12) to convert the expressions into dimensional forms. The two possible ferromagnetic states are abbreviated as F1 and F2, while P and AFM stand for the polar state and the antiferromagnetic state, respectively. The energy expressions and the density expressions for PM and APM states are identical. However, PM and APM states are restricted in space where the APM state exists if the absolute value of the linear Zeeman term is higher than that of the quadratic Zeeman term and the PM state exists otherwise.

States	Variation of density	Energy density	Restriction
(1,0,0) F1	$(\lambda_0+\lambda_1)u(\zeta) = \mu' + p' - q' - \zeta^2/2$	$\frac{[\zeta^2/2-p'+q'][\mu'+p'-q'-\zeta^2/2]}{(\lambda_0+\lambda_1)} + \frac{[\mu'+p'-q'-\zeta^2/2]^2}{2(\lambda_0+\lambda_1)}$	none
(0,1,0) P	$\lambda_0 u(\zeta) = \mu' - \zeta^2/2$	$\frac{\zeta^2/2[\mu'-\zeta^2/2]}{\lambda_0} + \frac{[\mu'-\zeta^2/2]^2}{2\lambda_0}$	none
(0,0,1) F2	$(\lambda_0+\lambda_1)u(\zeta) = \mu' - p' - q' - \zeta^2/2$	$\frac{[\zeta^2/2+p'+q'][\mu'-p'-q'-\zeta^2/2)]}{(\lambda_0+\lambda_1)} + \frac{[\mu'-p'-q'-\zeta^2/2]^2}{2(\lambda_0+\lambda_1)}$	none
(1,0,1) AFM	$\lambda_0 u(\zeta) = \mu' - q' - \zeta^2/2$ and $(u_1 - u_{-1}) \equiv F_z = \frac{p'}{\lambda_1}$	$\frac{[\zeta^2/2+q'][\mu'-q'-\zeta^2/2]}{\lambda_0} + \frac{[\mu'-q'-\zeta^2/2]^2}{2\lambda_0} - \frac{p'^2}{2\lambda_1}$	none
(1,1,1) (A)PM	$(\lambda_0+\lambda_1)u(\zeta) = k_1 - \zeta^2/2$ where $k_1 = \mu' + \frac{(p'^2-q'^2)}{2q'}$	$\frac{\zeta^2/2[k_1-\zeta^2/2)]}{\lambda_0+\lambda_1} + \frac{\lambda_1}{2}\left[\frac{k_1-\zeta^2/2}{\lambda_0+\lambda_1} - \frac{p'^2-q'^2}{2q'\lambda_1}\right]^2 + \frac{\lambda_0}{2}\left[\frac{k_1-\zeta^2/2}{\lambda_0+\lambda_1}\right]^2$	$PM(\lvert p'\rvert < \lvert q'\rvert)$ $APM \quad (\lvert p'\rvert > \lvert q'\rvert)$

direction, $\omega_x = 2\pi \times 50$ Hz, and the geometric mean of the trapping frequencies along the transverse direction, $\omega_{yz} = 2\pi \times 1261$ Hz. In Ref. [56], it was shown that for one-dimensional (1D) trapping geometry with the same trapping frequency, the TF approximation gives reasonably good results in predicting the number density for single-component stationary states for $N \geqslant 500$ in the absence of a magnetic field. There is reason to believe that the TF approximation might produce fairly accurate results for multicomponent stationary states in the presence of a small magnetic field if $N \geqslant 500$. For the following case studies, the number of condensate particles is fixed at $N = 5000$ for which the TF approximation should produce even better results. However, in what follows we will show that even at such a high particle number, TF-approximated results falter and corrections are needed.

Our present focus is on the PM state which is a multicomponent state that appears as a ground state for a range of p and q values in condensates with the ferromagnetic spin-spin interaction, e.g., ^{87}Rb. The antiferromagnetic state that becomes the ground state for ^{23}Na where the spin-spin interaction is of antiferromagnetic type [62] is also discussed in this paper. Note that the quasi-one-dimensional confinement is taken for convenience in numerical simulation.

A. PM state: TF approximation

For a ^{87}Rb condensate with ferromagnetic-type interaction, the numerical values of the parameters corresponding to the trap geometry are $l_x = 1.53$ μm, $l_{yz} = 0.30$ μm, $\lambda_0 = 17.66 \times 10^{-2}$, and $\lambda_1 = -6.22 \times 10^{-4}$. In this section, to compare the TF-approximated result with the numerical profile, as a case study, the linear and quadratic Zeeman terms are fixed at $p' = 0.01$ and $q' = 0.3$. The stationary state that is energetically favorable to be the ground state at these parameter values is the PM state. Note that the conclusions, however, are not dependent on a specific choice of parameter values but rather will remain valid for a range of p' and q' values for which the PM state is favorable as the ground state.

The subcomponent number densities of the PM state are [45]

$$u_1^{\mathrm{TF}} = \frac{(p'+q')^2}{4q'^2}\left[\frac{\mu' + \frac{(p'^2-q'^2)}{2q'} - \frac{1}{2}\zeta^2}{\lambda_0+\lambda_1} + \frac{q'^2-p'^2}{2\lambda_1 q'}\right], \quad (15)$$

$$u_{-1}^{\mathrm{TF}} = \frac{(p'-q')^2}{4q'^2}\left[\frac{\mu' + \frac{(p'^2-q'^2)}{2q'} - \frac{1}{2}\zeta^2}{\lambda_0+\lambda_1} + \frac{q'^2-p'^2}{2\lambda_1 q'}\right], \quad (16)$$

$$u_0^{\mathrm{TF}} = \frac{(q'^2-p'^2)}{2q'^2}\left[\frac{\mu' + \frac{(p'^2-q'^2)}{2q'} - \frac{1}{2}\zeta^2}{\lambda_0+\lambda_1} - \frac{q'^2+p'^2}{2\lambda_1 q'}\right], \quad (17)$$

which can be compared with the numerically simulated profiles. For the purpose of numerical simulation, imaginary time propagation in the split-step Fourier method [71] is used. The number density profiles as predicted by the TF approximation are used as initial seeds.

Comparison of the subcomponent densities of TF-approximated profiles with the numerical ones reveals very good agreement for the subcomponents u_1 and u_{-1}. The profile for the u_0 component also agrees in the high-density region of the trap [Fig. 1(a)], but starts to deviate when the other components u_1 and u_{-1} vanish, which for these parameter values is at around $\zeta_{\pm1}^{\mathrm{TF}} = \pm 10.3$. Note that $\zeta_{\pm1}^{\mathrm{TF}}$ is the TF radius of the $u_{\pm1}$ components. The numerical results suggest that the u_0 component falls much more sharply for $|\zeta| > |\zeta_{\pm1}^{\mathrm{TF}}|$ than the TF-approximated profile of the u_0 component [Eq. (17)]. Naturally, one might expect that, beyond the point $\zeta_{\pm1}^{\mathrm{TF}}$, the summation of the TF-approximated subcomponent number densities (i.e., $u_{\mathrm{tot}} = u_1 + u_0 + u_{-1}$ with $u_{\pm1} = 0$ for $|\zeta| > |\zeta_{\pm1}^{\mathrm{TF}}|$) will not agree with the numerical profile as there is a significant mismatch in the u_0 component.

This is quite natural as the PM state is only valid as long as all the subcomponents are populated. However, according to the TF approximation, the $u_{\pm1}$ components vanish at $\zeta = 10.3$, which is the TF radius of these two subcomponents. So, within the TF approximation, it can be said that near the center

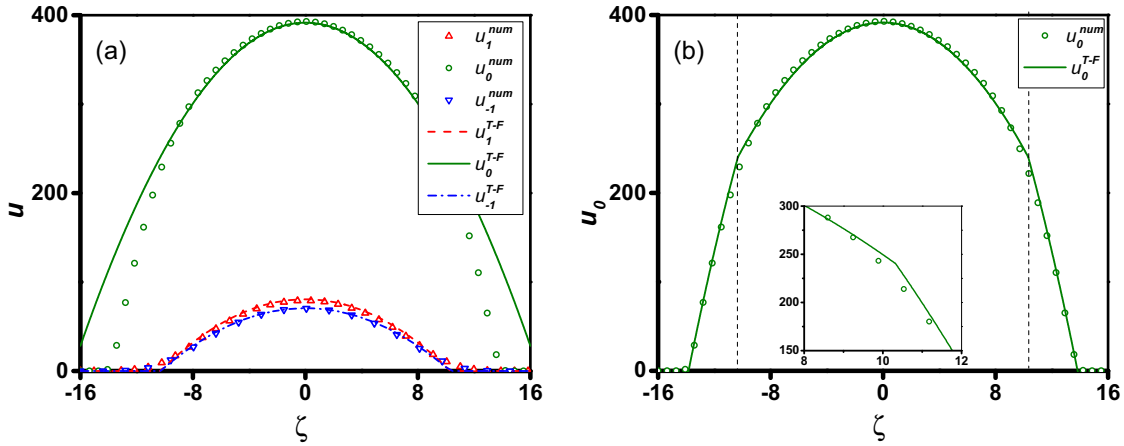

FIG. 1. (a) The TF-approximated subcomponent number densities for the PM state are compared with the numerical densities for the parameter values (dimensionless) $p' = 0.01$, $q' = 0.3$, $\lambda_0 = 17.66 \times 10^{-2}$, and $\lambda_1 = -6.22 \times 10^{-4}$. In this and all subsequent figures (unless otherwise specified), the numerical profile of u_1, u_0, and u_{-1} is shown in red triangles, green circles, and blue inverted triangles, respectively, while the analytical profile (in this figure, the TF profile) is shown in red dashed, green solid, and blue dash-dotted lines, respectively. The TF-approximated u_0 expression corresponding to the PM state starts to disagree with that of the numerical simulation beyond $|\zeta| > 10.3$, which is the TF radius of the $u_{\pm1}$ component. The dimensionless quantity $|\zeta|$ represents the distance from the center of the trap. (b) The analytical profile of the u_0 component corresponding to the TF-predicted domain structure and the numerically estimated u_0 are plotted against the distance from the trap center. The analytical profile of the u_0 follows the TF expression of the PM state when all the subcomponents are populated, i.e., $|\zeta| < |\zeta_{\pm1}^{\rm TF}|$, followed by the TF expression of the polar state. Dashed lines are placed at the TF radius $\zeta_{\pm1}^{\rm TF} = \pm 10.3$, which marks the domain boundary. Note that a discontinuity appears in the analytical u_0 at the domain boundary (inset) while the numerical profile is smooth. In this and in subsequent figures, the quantities u_1, u_0, u_{-1}, and ζ are dimensionless.

of the harmonic trap, the PM state is occupied, and beyond the TF radius of $u_{\pm1}$, the PM state ceases to exist. In this region, only the u_0 component is present, which signifies that it is (0,1,0) or the polar state (see Table I) that occupies the low-density region of the trap.

The subcomponent number densities for such a construct can be given as

$$u_1^{\rm TF} = \frac{(p'+q')^2}{4q'^2}\left[\frac{\mu' + \frac{(p'^2-q'^2)}{2q'} - \frac{1}{2}\zeta^2}{\lambda_0+\lambda_1} + \frac{q'^2-p'^2}{2\lambda_1 q'}\right], \quad (18)$$

$$u_{-1}^{\rm TF} = \frac{(p'-q')^2}{4q'^2}\left[\frac{\mu' + \frac{(p'^2-q'^2)}{2q'} - \frac{1}{2}\zeta^2}{\lambda_0+\lambda_1} + \frac{q'^2-p'^2}{2\lambda_1 q'}\right],$$

$$u_0^{\rm TF} = \begin{cases} \frac{(q'^2-p'^2)}{2q'^2}\left[\frac{\mu' + \frac{(p'^2-q'^2)}{2q'} - \frac{1}{2}\zeta^2}{\lambda_0+\lambda_1} - \frac{q'^2+p'^2}{2\lambda_1 q'}\right] & \text{if } |\zeta| \leqslant \left|\zeta_{\pm1}^{TF}\right| \\ \frac{\mu'_{\rm polar} - \frac{1}{2}\zeta^2}{\lambda_0} & \text{otherwise.} \end{cases} \quad (19)$$

Note that, additionally for the stability of the domain structure, the chemical potentials of the PM state (μ') and that of the polar state ($\mu'_{\rm polar}$) have to be the same. For $N = 5000$, the chemical potential comes out to be $\mu' = \mu'_{\rm polar} = 95.63$. As can be seen in Fig. 1(b) this domainlike explanation works really well as we compare the subcomponent density with the numerical u_0, but there is a discontinuity at $|\zeta| = |\zeta_{\pm1}^{\rm TF}|$. The slope of analytical u_0 also changes drastically around this point, resulting in a lot of kinetic energy cost. The sharper decrease of the u_0 component happens as the TF radius of the polar state is much lower than the projected TF radius of the u_0 of the PM state.

The above conclusion about the discontinuity in the u_0 component and hence the limitations of the TF approximation can be further strengthened if we compare numerical simulation and TF-approximated prediction for a different spin-spin interaction, $c_1 \to 5c_1^{\rm Rb}$, while keeping all other parameter values the same. Experimentally, this is possible via Feshbach resonance [72]. This corresponds to a change in $\lambda_1 = -3.11 \times 10^{-3}$ for the same spin-independent interaction term, $\lambda_0 = 17.66 \times 10^{-2}$. We numerically simulate the condensate profile for these interaction parameters and for the same and $p' = 0.01$ and $q' = 0.3$ to compare it with the domainlike prediction of the TF approximation.

For this choice of parameter values, the domainlike structure predicted by the TF approximation, with $\mu' = \mu'_{\rm polar} = 94.73$, has a similar discontinuity (Fig. 2) for the subcomponent u_0 at $|\zeta| = |\zeta_{\pm1}^{\rm TF}| = 13.13$. The total density for this domainlike structure will also have that same discontinuity. Note that the numerical profile of the condensate (specifically of the u_0 component) is smooth and does not show any discontinuity in Figs. 1 and 2. The numerical data suggest a non-negligible presence of the $u_{\pm1}$ beyond their TF radius $|\zeta_{\pm1}^{\rm TF}|$. Additionally, from the numerical data we find that the phase-matching condition, i.e., $\theta_r \simeq 0$, is satisfied throughout the trap, which indicates that the PM state is the only ground state that is present in all regions of the trap.

B. PM state: The variational method

In Ref. [56], a multimodal variational method was introduced which incorporates the kinetic energy contribution and produces the subcomponent number density profiles of a stationary state with great accuracy. The variational method (VM) was developed for a spin-1 BEC in the absence of a

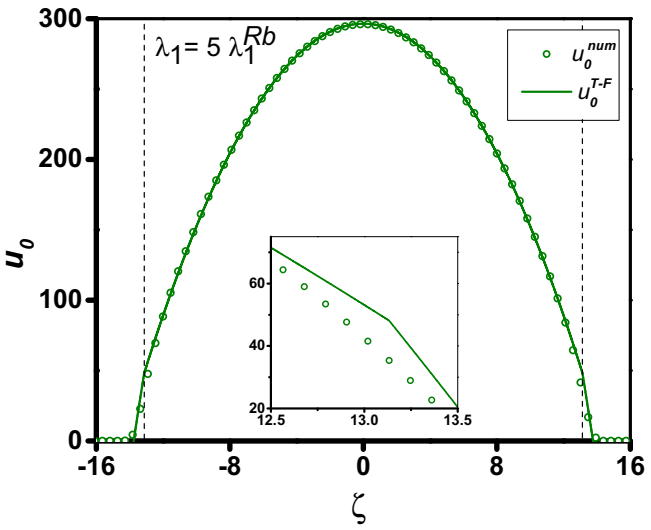

FIG. 2. The subcomponent u_0 for the TF-approximated PM-polar domains (green solid line) is compared with the numerical profile (green circles) for the same $p' = 0.01$ and $q' = 0.3$ and $\lambda_0 = 17.66 \times 10^{-2}$ with a different spin-dependent interaction coefficient, $\lambda_1 = -3.11 \times 10^{-3}$, which is now five times λ_1 corresponding to ^{87}Rb for this trap geometry. The analytical u_0 follows the TF profile of the PM state near the center of the trap, and the TF profile of the polar state beyond $|\zeta_{\pm1}^{\rm TF}| = 13.13$ (vertical dashed lines mark this point). The analytical profile of the u_0, corresponding to the domain structure, has a distinct discontinuity at $|\zeta_{\pm1}^{\rm TF}|$ (see inset).

magnetic field, which works really well even for condensates with a small number of particles where the TF approximation was shown to be no longer valid. The PM state was also analyzed using the multimodal VM, but for $p = 0$ and $q = 0$, the subcomponents of the PM state follow the same spatial mode, which reduces the complexity significantly.

We extend the same procedure here in presence of a magnetic field. If the subcomponents do not follow the same spatial variation, the situation is much more complex but the extended VM tackles it with ease. In this section we will briefly discuss the procedure; for a more elaborate description see Appendix A.

For the variational method to work, we assume the subcomponent densities as

$$u_{\pm1,0}^{\rm in} = g_{\pm1,0}(\mu', \zeta) \quad \text{for} \quad |\zeta| \leqslant \zeta_{\pm1,0}^{\rm mat}, \tag{20}$$

$$u_{\pm1,0}^{\rm out} = (a_{\pm1,0} + c_{\pm1,0}|\zeta| + d_{\pm1,0}\zeta^2) \exp\left(-\frac{\zeta^2}{b_{\pm1,0}}\right) \quad \text{for} \quad |\zeta| \geqslant \zeta_{\pm1,0}^{\rm mat}, \tag{21}$$

where $g_{\pm1,0}(\mu', \zeta)$ is the functional form of the subcomponent density $u_{\pm1,0}$ for a particular stationary state near the center of the trap, which is, as noted earlier, obtained from the solution of Eqs. (13) and (14), neglecting the Laplacian term [for the functional form of $g_{\pm1,0}(\mu', \zeta)$ for the PM state please see Eqs. (A4)–(A6) in Appendix A]. In the low-density region, we assume the number density (or the wave function) taking into account the first few lowest harmonic oscillator states.

To determine the unknown coefficients a_m, b_m, c_m, and d_m with $m = \pm1, 0$, we impose a smooth matching condition at $|\zeta| = \zeta^{\rm mat}$ where the $\sqrt{u_{\pm1,0}}$ and their first three derivatives become equal for low- and high-density expressions. The third derivative matching also ensures a smooth kinetic energy profile. From these four conditions, one can determine all four coefficients appearing in Eq. (21), which now become functions of μ' and $\zeta_{\pm1,0}^{\rm mat}$. If we integrate the subcomponent densities and add them, the result would correspond to the total number of condensate particles. From this number conservation equation, the parameter μ' can be expressed in terms of $\zeta_{\pm1,0}^{\rm mat}$ (see Appendix A for more details). Following this step, the densities and thus the total energy can be written only as a function of the matching points $\zeta_{\pm1,0}^{\rm mat}$ which are the only variables left. The matching points can be found from the minimization of the total energy. Once the matching points are obtained, we can write the analytical expressions for all the subcomponent densities.

Before we implement the VM, note that if we add the TF-approximated subcomponent densities of the PM state given by Eqs. (15)–(17), we arrive at the total number density,

$$u_{\rm tot}^{\rm PM} = \frac{\mu' + \frac{(p^2-q^2)}{2q} - \frac{1}{2}\zeta^2}{\lambda_0 + \lambda_1}. \tag{22}$$

This expression of the total TF-approximated density has a curious character. The number densities of the individual components $u_{\pm1}^{\rm TF}$ reach zero at a radius $|\zeta| = |\zeta_{\pm1}^{\rm TF}|$, which is smaller than the radius where the $u_0^{\rm TF}$ comes to zero. However, beyond $|\zeta| = |\zeta_{\pm1}^{\rm TF}|$, the expression of $u_{\rm tot}^{\rm PM}$ keeps on counting the negative contribution of densities $u_{\pm1}^{\rm TF}$ [Eqs. (15) and (16)] until the $u_0^{\rm TF}$ component [Eq. (17)] reaches zero to conserve the number of particles under the TF approximation. Thus, the $u_0^{\rm TF}$ that exists in the TF approximation beyond $|\zeta_{\pm1}^{\rm TF}|$ is actually an overcount to which, when the negative densities of $u_{\pm1}^{\rm TF}$ add up, it gives a total density according to Eq. (22). This is a feature of the TF approximation.

This shows up clearly in the TF-approximated expression of the u_0 component [Eq. (17)] deviating from the numerical estimation [Fig. 1(a)] beyond the TF radius $|\zeta_{\pm1}^{\rm TF}|$ beyond which $u_{\pm1}^{\rm TF} < 0$ [in Eqs. (15) and (16)]. However, the TF-approximated total density [Eq. (22)] is seen in Fig. 3 to match the numerical profile when the negative densities $u_{\pm1}^{\rm TF} < 0$ are added to the TF-approximation prescribed u_0. Since we build the VM solution with a reference to the TF-approximated profile at the core, in what follows we will use $u_{\pm1}^{\rm TF}$ and the density profile $u_{\rm tot}^{\rm PM}$ to develop VM in a multimodal approach. This approach would work fine, but not the one that includes $u_0^{\rm TF}$ in the place of $u_{\rm tot}^{\rm PM}$, because $u_0^{\rm TF}$ is an overcount beyond $|\zeta_{\pm1}^{\rm TF}|$. The expression of u_0 can be later found out by subtracting the sum of variational profiles of $u_{\pm1}$ from the total number density profile, i.e., $u_0^{\rm VM} = u_{\rm tot}^{\rm VM} - u_1^{\rm VM} - u_{-1}^{\rm VM}$. Note that, for the PM state, the spatial mode for the u_1 and u_{-1} are equivalent, so the matching point for those two subcomponents will be the same, i.e., $\zeta_1^{\rm mat} = \zeta_{-1}^{\rm mat}$. Thus, the minimization of the total energy in the two-dimensional parameter space of $\zeta_1^{\rm mat}$ and $\zeta_{\rm tot}^{\rm mat}$ will determine the energy itself as well as approximate values of these parameters.

For this particular case, we find that $\zeta_{\pm1}^{\rm mat} = 8.5$ and $\zeta_{\rm tot}^{\rm mat} = 13.43$ minimizes the total energy. These matching points

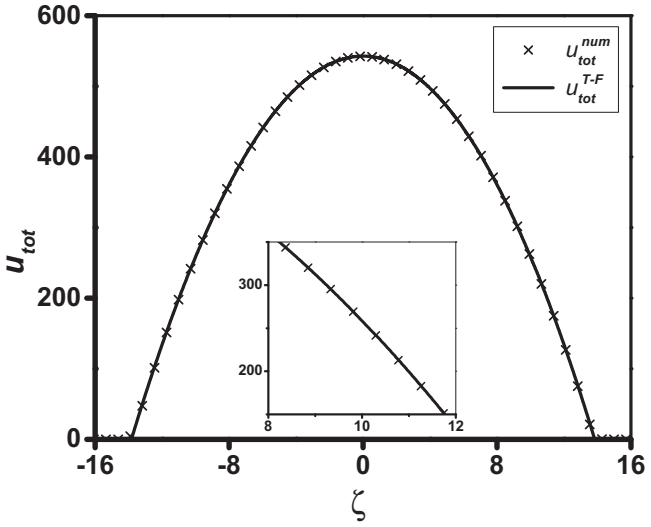

FIG. 3. The total density (dimensionless) obtained from numerical simulation (for $p' = 0.01$, $q' = 0.3$, $\lambda_0 = 17.66 \times 10^{-2}$, and $\lambda_1 = -6.22 \times 10^{-4}$) matches quite well with Eq. (22), which is the TF-approximated expression corresponding to the total density of the PM state. This expression of total number density is only valid as long as all the subcomponents are populated. Beyond $|\zeta_{\pm1}^{\rm TF}|$, Eq. (22) incorporates the negative density contribution from $u_{\pm1}^{\rm TF}$. Inset: The same expression matches with the numerical total density even beyond the TF radius $|\zeta_{\pm1}^{\rm TF}| \simeq 10.3$.

also determine the parameter $\mu' = 95.6$ from the number conservation equation. Thus, number densities can be written in an analytical form as

$$u_1^{\rm VM} = \begin{cases} 1.5173(53.1007 - 0.5\zeta^2) & \text{if } |\zeta| \leqslant 8.5 \\ 1.5173(114177.278 - 31226.158|\zeta| \\ \qquad + 2184.067\zeta^2)\exp(-0.0824\zeta^2) & \text{otherwise,} \end{cases} \tag{23}$$

$$u_{-1}^{\rm VM} = \begin{cases} 1.3278(53.1007 - 0.5\zeta^2) & \text{if } |\zeta| \leqslant 8.5 \\ 1.3278(114177.278 - 31226.158|\zeta| \\ \qquad + 2184.067\zeta^2)\exp(-0.0824\zeta^2) & \text{otherwise,} \end{cases} \tag{24}$$

$$u_{\rm tot}^{\rm VM} = \begin{cases} 5.6839(95.4599 - 0.5\zeta^2) & \text{if } |\zeta| \leqslant 13.425 \\ 5.6839(4.8883 \times 10^{25} - 7.4283 \times 10^{24}|\zeta| \\ \qquad + 2.8227 \times 10^{23}\zeta^2)\exp(-0.2779\zeta^2) & \text{otherwise,} \end{cases} \tag{25}$$

where the numbers are rounded up to four decimal places. The analytical expressions of the subcomponent densities obtained from the VM is in excellent agreement with the numerical profiles [see Fig. 4(a)]. Note that in Eq. (25) the coefficients of the total number density might look very large, but for $|\zeta| \geqslant 13.43$ where the expression is valid, the contribution from the exponential part is so small that the combined contribution asymptotically goes to zero at large distances and matches quite accurately with the numerical profile [see the inset of Fig. 4(b)].

We have made a case study of the PM state, a multicomponent stationary state that becomes the ground state for a range of linear and quadratic Zeeman strengths. For the purpose of comparison with numerical simulation, we have chosen 1D harmonic trapping and particular values of p', q', and the number of condensate particles, N. The procedure and the conclusions do not depend on the particular choices of these parameters and are valid as long as the PM state is favored to be the ground state.

As the GP equations are coupled, the low-density behavior of $u_{\pm1}$ stemming from the Laplacian term [Eqs. (13) and (14)] cannot be neglected and it affects the u_0 component [Eq. (13)] as well. The variational method accurately estimates the effect

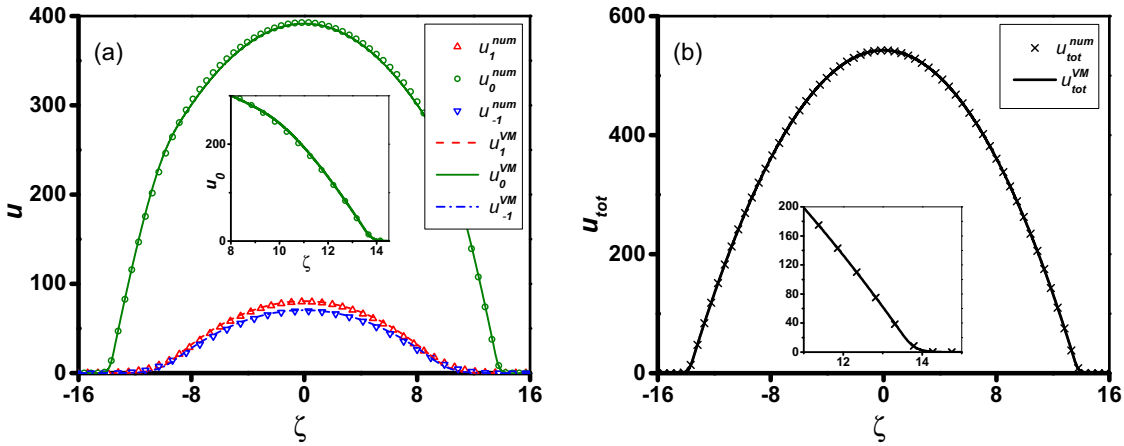

FIG. 4. (a) The subcomponent number density of the PM state obtained via the numerical and variational methods is plotted against the distance from the trap center ζ, for $p' = 0.01$, $q' = 0.3$, $\lambda_0 = 17.66 \times 10^{-2}$, and $\lambda_1 = -6.22 \times 10^{-4}$. The VM produces a very good analytical profile that describes the numerical data quite well even in the tail part of the condensate. The VM rules out any domainlike possibility and analytically estimates the u_0 component that is quite accurate in comparison to the numerical profile (see inset). (b) The VM provides an excellent analytical profile of the total density to match the numerical result near the core of the trap as well as in the low-density region (inset), where it gives an analytic estimate of the condensate density which asymptotically goes to zero at a large distance.

of the Laplacian term and estimates $u_{\pm1}$ in the low-density region of the trap. Note that the PM state can only be present as long as all the subcomponents are populated. Beyond $\zeta_{\pm1}^{\rm TF}$, according to the TF approximation, the $u_{\pm1}$ components are zero, which indicates the polar state being occupied there, whereas the finite presence of these components beyond $\zeta_{\pm1}^{\rm TF}$, which the VM estimates, indicates that the PM state is present throughout the trap, which numerical results also validate. Note that the VM is an approximation scheme that works really well in estimating the subcomponent number densities (also the mean fields), which produces a very good estimation of the vector order parameter of the spin-1 system. Like other approximate methods, it has some limitations as well. For example, at a large distance from the center of the trap (very large ζ), where the total density $u_{\rm tot}^{\rm VM}$ and $u_{\pm1}^{\rm VM}$ are very close to zero and can be considered negligible, we find that the total density is slightly lesser than the combined contribution of the ±1 subcomponents, hence making $u_0^{\rm VM}$ slightly negative which is not physical. For this reason, we have taken the contribution up to a large ζ after which we assume that u_0 goes to zero. Thus the kinetic energy contribution is included and considered up to a large distance without discontinuity.

Note that, the ratio of the spin-dependent and spin-independent interaction coefficients, for ^{87}Rb, is really small ($|\lambda_1|/\lambda_0 \sim 1/300$). The spin-spin interaction affects the subcomponent density distributions. As a result, a natural query may arise about what would happen if $|\lambda_1|$ and λ_0 are of comparable strength. We verified that the accuracy of the variational method remains unaffected in such a situation even when there is a sufficient increment in the strength of the Zeeman terms (see Fig. 11 in Appendix A).

Comparison with single-mode approximation (SMA)

The single-mode approximation is a widely adopted method for the study of spin-oscillation dynamics in spinor condensates. Under the SMA, all the subcomponents are assumed to follow the same spatial variation [62],

$$\psi_m(\vec{r},t) = \sqrt{N}\xi_m(t)\psi_{\rm SMA}(\vec{r})\exp\left(-\frac{i\mu t}{\hbar}\right), \tag{26}$$

where $\psi_{\rm SMA}(\vec{r})$ is the spatial mode and $\xi_m(t)$ is, in general, a complex quantity that obeys $\sum_{m=-1}^{m=1}|\xi_m(t)|^2 = 1$. For 1D harmonic confinement, one can use the same scaling as in Eqs. (11) and (12), where

$$\psi_{\rm SMA}(\zeta) = \sqrt{2\pi l_{yz}^2 l_x}\psi_{\rm SMA}(\vec{r}). \tag{27}$$

The mode function $\psi_{\rm SMA}(\zeta)$ can be determined by solving

$$\left[-\frac{1}{2}\frac{d^2}{d\zeta^2} + \frac{1}{2}\zeta^2 + \lambda_0 N|\psi_{\rm SMA}(\zeta)|^2\right]\psi_{\rm SMA}(\zeta) = \mu'\psi_{\rm SMA}(\zeta), \tag{28}$$

subjected to the constraint

$$\int_0^\infty d\zeta|\psi_{\rm SMA}(\zeta)|^2 = 1. \tag{29}$$

The solution of the equations

$$i\frac{d\xi_{\pm1}}{d\tau} = (\mp p' + q')\xi_{\pm1} + \tilde{\lambda}_1\left[(\rho_{\pm1}+\rho_0-\rho_{\mp1})\xi_{\pm1} + \xi_0^2\xi_{\mp1}^*\right], \tag{30}$$

$$i\frac{d\xi_0}{d\tau} = \tilde{\lambda}_1[(\rho_1+\rho_1)\xi_0 + 2\xi_1\xi_{-1}\xi_0^*], \tag{31}$$

provides the dynamics of the normalized spinor ξ_m, where $\rho_m \equiv |\xi_m(t)|^2$ and τ is related to time t as, $\tau = \omega_x t$. The effective volume of the system, $V^{\rm eff} \equiv 4\pi l_x l_{yx}^2(\int_{-\infty}^{\infty} d\zeta\,|\psi_{\rm SMA}(\zeta)|^4)^{-1}$, determines the parameter $\tilde{\lambda}_1$ [62]:

$$\tilde{\lambda}_1 \equiv \frac{c_1 N}{\hbar\omega_x V^{\rm eff}} = \frac{\lambda_1 N}{2}\int_{-\infty}^{\infty} d\zeta\,|\psi_{\rm SMA}(\zeta)|^4. \tag{32}$$

Rewriting the normalized spinor,

$$\xi_m = \sqrt{\rho_m}\exp(-i\theta_m)\exp(ip'm\tau), \tag{33}$$

simplifies Eqs. (30) and (31),

$$\frac{d\rho_0}{d\tau} = -2\tilde{\lambda}_1\rho_0\sqrt{(1-\rho_0)^2 - f_z^2}\sin\theta_r, \tag{34}$$

$$\frac{d\theta_r}{d\tau} = -2\tilde{\lambda}_1\frac{(1-2\rho_0)(1-\rho_0) - f_z^2}{\sqrt{(1-\rho_0)^2 - f_z^2}}\cos\theta_r + 2q' - 2\tilde{\lambda}_1(1-2\rho_0), \tag{35}$$

where $f_z = |\xi_1|^2 - |\xi_{-1}|^2$, and θ_r is the relative phase. From ρ_0, one can get to the population fraction in the other two components, i.e., $\rho_{\pm1} = (1-\rho_0 \pm f_z)/2$ [62].

We select an experimentally relevant case of $p = 0$ and $q = 0.3$, which also corresponds to the PM state in the ground state, to compare the SMA with the numerical results. The numerical solution of Eq. (28) estimates the mode function which is the same for all the spin components under the SMA. Following that, the stationarity condition can be employed in Eqs. (34) and (35) to find the population fraction for different subcomponents. When $f_z = 0$, for PM state ($\theta_r = 0$), we find $\tilde{\lambda}_1 \simeq -0.2703$, $\rho_0 \simeq 0.777$, and $\rho_{\pm1} \simeq 0.111$. These population fractions determine the subcomponent densities as $u_m^{\rm SMA} = N\rho_m|\psi_{\rm SMA}(\zeta)|^2$.

The total density profile obtained from the SMA ($N|\psi_{\rm SMA}(\zeta)|^2$) is in good agreement with the numerically obtained total number density. This is important for an accurate determination of $\tilde{\lambda}_1$ [Eq. (32)]. Still, the subcomponent density profiles as obtained from the SMA do not agree with the numerically obtained profiles [see Fig. 5(a)]. Note that it is well known that the SMA is not exact, even in the ground state for the PM state, which is also known as the broken-axisymmetry phase [62]. The inaccuracy of SMA further emphasizes the fact that the subcomponents do not follow a single spatial mode for the PM state. Thus, a multimodal analysis is required. In Fig. 5(b) we demonstrate that the subcomponent density distribution with $\zeta_{\pm1}^{\rm mat} = 8.495$ and $\zeta_{tot}^{\rm mat} = 13.425$ and $\mu' = 95.46$ as obtained from the multimodal VM is in excellent agreement with the numerical simulation for this experimentally relevant case.

In the next section, we will do a brief case study on the antiferromagnetic state which is the other possible multicomponent stationary state that becomes the ground state for ^{23}Na.

C. Antiferromagnetic state

For the ^{23}Na condensate, we set the same trapping frequencies corresponding to 1D confinement as mentioned earlier for the ferromagnetic-type condensate. The oscillator length in

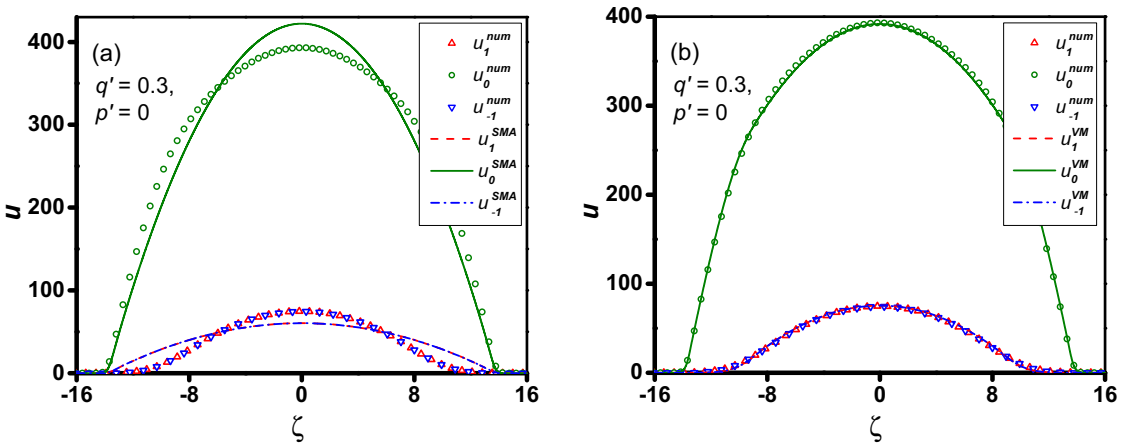

FIG. 5. (a) The subcomponent density profiles obtained from the SMA are compared with the numerical profiles for $p' = 0$, $q' = 0.3$, $\lambda_0 = 17.66 \times 10^{-2}$, and $\lambda_1 = -6.22 \times 10^{-4}$. Though the SMA estimated total number density profile agrees with the numerical total number density distribution (not shown here), the subcomponent density profiles are not in agreement. (b) The VM-estimated subcomponent profiles with $\zeta_{\pm 1}^{\rm mat} = 8.495$ and $\zeta_{\rm tot}^{\rm mat} = 13.425$ and $\mu' = 95.46$ for the case of $p' = 0$ and $q' = 0.3$ match quite well with the multimodal distribution obtained from the numerical estimation.

the elongated direction is $l_x = 2.97$ μm, and in the transverse direction is $l_{yz} = 0.59$ μm. Note that, although we consider the same trapping geometry, the oscillator length scales for ^{23}Na and ^{87}Rb condensates are different due to the different masses of the species. The spin-independent and spin-spin interaction parameters are $\lambda_0 = 46.16 \times 10^{-3}$ and $\lambda_1 = 7.43 \times 10^{-4}$ corresponding to the values given in Ref. [62]. The positive spin-spin interaction coefficient signifies the antiferromagnetic type of spin interaction for the ^{23}Na condensate. For a range of linear and quadratic Zeeman terms, the antiferromagnetic (AFM) state is found to be favorable as the ground state, but for the purpose of numerical study, we will focus on the case where $p' = 0.2$ and $q' = -0.5$.

As long as the u_1 and u_{-1} subcomponents are nonzero, the TF approximation gives an estimation of the total as well as subcomponent number densities (see Table I),

$$u_1^{\rm TF} = \frac{\mu' - q' - \zeta^2/2}{2\lambda_0} + \frac{p'}{2\lambda_1}, \tag{36}$$

$$u_{-1}^{\rm TF} = \frac{\mu' - q' - \zeta^2/2}{2\lambda_0} - \frac{p'}{2\lambda_1}. \tag{37}$$

As the chosen value of p' is positive (also, $\lambda_1 > 0$), the u_{-1} component goes to zero much faster than the other one. So beyond the TF radius of the u_{-1} component, the AFM state ceases to exist but the sole presence of the u_1 component signifies the ferromagnetic state. So according to the TF approximation, the situation is domainlike with the AFM state at the center of the trap followed by the ferromagnetic state outside (for $|\zeta| > \zeta_{-1}^{TF}$).

Similar to the case for the PM state that we have seen earlier, the numerical simulation does not vindicate the domainlike prediction; rather the AFM state is found to be present for all values of ζ. Following the same procedure as described for the PM state, one can apply the VM for the total density and the subcomponent density u_{-1}. The u_0 component is empty and there will be two matching points $\zeta_{tot}^{\rm mat}$ and $\zeta_{-1}^{\rm mat}$ which are to be found out from the minimization of the total energy. For the previously mentioned p' and q' values, we get these two matching points to be $\zeta_{tot}^{\rm mat} = 8.36$ and $\zeta_{-1}^{\rm mat} = 6.08$. These also produce the analytical formulas of the total density and the u_{-1} components. The density expression for the u_1 component is obtained by subtracting the other subcomponent u_{-1} from the total density.

The VM shows that the domainlike situation that the TF approximation predicts is incorrect and justifies the fact that the kinetic energy terms cannot be neglected near the TF radius for the subcomponent which is of smaller density—in this case, the u_{-1} component. The VM also produces a low-density expression of the u_{-1} component which has a small but nonzero presence beyond $u_{-1}^{\rm TF}$. Thus, it is only the AFM state that is present for all regions of space. Moreover, the analytic number density expressions obtained from VM corresponding to each subcomponent are in fair agreement with the numerically obtained profiles (see Fig. 6).

IV. PHASE TRANSITION BETWEEN PM AND POLAR STATES UNDER CONFINEMENT

In the previous section, we have shown that the results of the TF approximation and the SMA are inaccurate for the multicomponent ground states under 1D harmonic confinement. The variational method, on the other hand, analytically obtains the correct profile of the condensate ground states (PM state) as opposed to the TF-approximated domains of PM and polar states.

Using this variational method one can estimate the phase transitions between different ground states of a trapped spin-1 BEC, especially when the multicomponent states are involved. We will choose the case of spin-1 BEC with the ferromagnetic type of spin-spin interaction inside a three-dimensional (3D) isotropic harmonic confinement. While the numerical simulation is costlier in higher dimensions, the VM can be implemented to analytically obtain the phase boundaries involving multicomponent states.

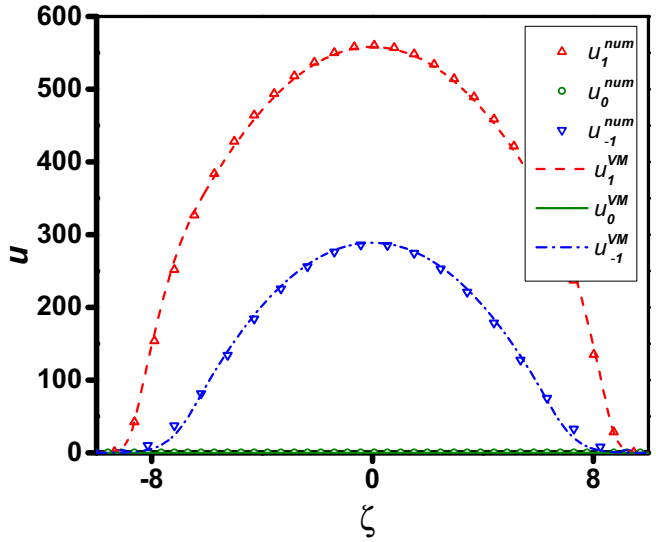

FIG. 6. Subcomponent density expressions obtained via VM are compared with the numerical profile for the antiferromagnetic state with the Zeeman terms fixed at $p' = 0.2$ and $q' = -0.5$ for $\lambda_0 = 46.16 \times 10^{-3}$ and $\lambda_1 = 7.43 \times 10^{-4}$.

In the absence of confinement (hence, a constant number density), the phase diagram for the homogeneous spin-1 condensate is well known. When the spin-spin interaction is of ferromagnetic type ($c_1 < 0$), the phase diagram of the homogeneous condensate, Fig. 7 [62], shows different stationary states favorable as the ground state in certain regions of the

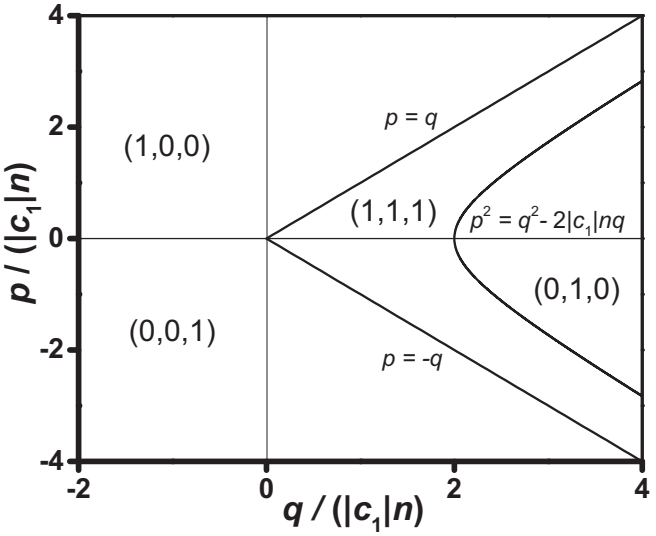

FIG. 7. The phase diagram of the spin-1 condensate with a ferromagnetic type of spin-spin interaction ($c_1 < 0$) in the absence of any confinement. The ferromagnetic, PM, and polar states are favorable to become the ground states depending on the linear and quadratic Zeeman terms, p and q. The number density n, being a constant over space in the absence of any confinement, can be used to scale the p and q axes. In this scaling, the phase diagram becomes universal in the sense that this diagram does not change for a change in number density (constant over space, i.e., homogeneous). The quantities $p/(|c_1|n)$ and $q/(|c_1|n)$ are dimensionless.

q, p parameter space. For the negative quadratic Zeeman term, the ferromagnetic states are the ground states, where one of them is favorable depending on the sign of the linear Zeeman term. In the positive half, if the quadratic Zeeman term is greater than the absolute value of the linear term (i.e., $q \geqslant |p|$) then the PM state becomes the ground state as long as $p^2 \geqslant q^2 - 2|c_1|nq$ is satisfied, followed by the polar state in the remaining part of the q, p parameter space. For the homogeneous condensate, the PM-polar phase transition occurs at $p^2 = q^2 - 2|c_1|nq$.

For an isotropic 3D confinement of trapping frequency ω, we scale the number density and the interaction parameters as

$$c_0 = \frac{4\pi}{3} l_{\rm osc}^3 \lambda_0 \hbar\omega, \quad c_1 = \frac{4\pi}{3} l_{\rm osc}^3 \lambda_1 \hbar\omega, \tag{38}$$

$$u_m = \frac{4\pi}{3} l_{\rm osc}^3 n_m, \quad r = l_{\rm osc}\zeta, \tag{39}$$

where, $l_{\rm osc}^2 = \hbar/(m\omega)$ is the oscillator length scale for this geometry. For this choice of scaling, the phase equations would assume a similar structure as in Eqs. (13) and (14) with the Laplacian term to be replaced with $-\frac{1}{2}\frac{1}{\zeta^2}\frac{d}{d\zeta}(\zeta^2\frac{d}{d\zeta})$, the radial part (of the Laplacian) in the spherical polar coordinate (see Appendix B for details).

We first implement the VM for a condensate under a 3D isotropic harmonic confinement of trapping frequency $\omega = 2\pi \times 100$ Hz. For ^{87}Rb, the oscillator length scale corresponding to this choice of trapping frequency is $l_{\rm osc} = 1.07$ μm and the corresponding interaction parameters defined in Eqs. (38) and (39) are $\lambda_0 = 1.484 \times 10^{-2}$ and $\lambda_1 = -5.249 \times 10^{-5}$.

The VM estimates total energy of the polar state (see Appendix B) and the PM state for different p' and q', a comparison of which would reveal the phase boundary for the trapped condensate. For a homogeneous condensate, if we look at the energy difference between these two states for $p = 0$ [Fig. 8(a)], one can see that the energy of the PM state is lower than the polar state for small positive values of q. As the strength of the quadratic Zeeman term is increased, the energy difference reduces, and at the transition point $q_t^{\rm hom} = 2|c_1|n$, it vanishes.

The number density of the $m = \pm 1$ projection for the homogeneous case (Eq. 96 in Ref. [62]),

$$n_{\pm 1}|_{\rm hom} = \frac{(q \pm p)^2}{4q^2}\left(\frac{-p^2 + q^2 + 2c_1 nq}{2c_1 nq}\right) n, \tag{40}$$

decreases with increasing q at a constant p. For $p = 0$, this vanishes at $q = q_0^{\rm hom} = 2|c_1|n$, which is the same q value as that of the transition, i.e., $q_t^{\rm hom} = q_0^{\rm hom}$. Hence, beyond the phase boundary (also for $p \neq 0$), the PM state is nonexistent.

An equivalent of the $q_0^{\rm hom}$ for the trapped case can be estimated from the TF-approximated peak density, i.e., the number density at the center of the harmonic trap of the $u_{\pm 1}$ component. Note that the TF approximation is quite accurate near the center of the trap. We can also find the same from the VM, which would produce the same estimation as it is built with reference to the TF solution at the core. For simplicity, if we follow the TF profile, we can notice that the increment in q' would lower the peak density of the $u_{\pm}$ component as $\lambda_1 < 0$. The value of q' for which the peak density of the $u_{\pm 1}$

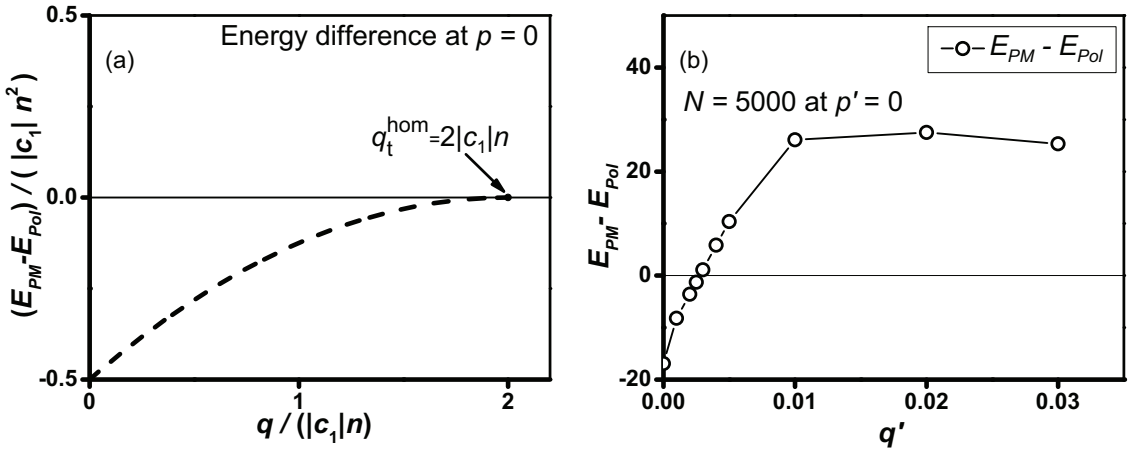

FIG. 8. (a) For condensates with the ferromagnetic type of spin-spin interaction ($c_1 < 0$), the energy difference of the PM and the polar states, scaled with the constant number density, is plotted against the variation of q at $p = 0$ for condensates in the absence of any trapping. The energy difference after scaling with $|c_1|n^2$ and $q/(|c_1|n)$, shown in the axes, is dimensionless. At $q \approx 0$, the energy corresponding to the PM state is lower than that of the polar state, making the PM state favorable to become the ground state. As q increases, the energy difference reduces, and at the transition point ($q_t^{\rm hom} = 2|c_1|n$ at $p = 0$), the PM state energy becomes equal to that of the polar state. At this point, the subcomponent density $n_{\pm 1}$ vanishes. Hence beyond this point, the PM state does not exist. (b) The VM estimated energy difference (dimensionless) between the PM and polar state under the 3D harmonic trapping for 5000 condensate particles with varying q' at $p' = 0$ (both are dimensionless). The total energy of the PM state is lower than that of the polar state for small values of the quadratic Zeeman term. The energy difference in the trapped situation indicates that the phase transition happens at $q' \simeq 0.0027$, which is much lower than $q' \simeq 0.0377$, beyond which the PM state ceases to exist.

vanishes (at $p' = 0$) is q_0^{tr} (tr in the superscript is shorthand for "trapped"), which is equivalent to $q_0^{\rm hom}$ of the homogeneous counterpart in the sense that, for the homogeneous case and TF as well, the PM state cannot exist beyond these values of q and q', respectively.

The VM estimated energy difference between the PM and the polar states [Fig. 8(b)] for $N = 5000$ indicates that the phase transition happens at $q_t^{tr} = 0.0027$, which is an order of magnitude lower than $q_0^{tr} \simeq 0.0377$. This means, unlike the homogeneous case where the PM state is favored as the ground state in its entire region of existence (for $q > 0$ and below $q_0^{\rm hom}$), the trapped situation is different and there exists a range of q' values ($q_t^{tr} < q' < q_0^{tr}$) for which the PM state, although present, is not selected as the ground state. This crucial result, i.e., $q_t^{tr} < q_0^{tr}$, that we analytically obtained via VM is also verified numerically in Appendix C.

As is evident from Fig. 7, for the homogeneous condensate, the constant number density is used in the scaling of p and q. As a result, the whole phase diagram is universal with respect to number density variation for any homogeneous spin-1 condensate with the ferromagnetic type of spin-spin interaction. In contrast, in the presence of confining potential, the number density varies over space and even the peak density (number density at the center of the trap) is different for different stationary states. In this case not the number density but the number of condensate particles is of importance.

For a choice of p', the VM is employed to estimate the q' value for which the energy difference of the PM and the polar states vanishes. Following the same procedure for different choices of p', one can get the phase boundaries [Fig. 9(a)] in the q', p' parameter space for a range of condensate particles. Note that these phase transition boundaries are similar and asymptotically approach the $|p'| = q'$ line for large values of q'. At the same value of the linear Zeeman term p', with an increase in the number of particles, the phase transition happens at a higher value of q'. For example, at $p' = 0$, the phase transition happens at $q_t^{tr} = 0.0027$ for 5000 particles, which gets shifted to $q_t^{tr} = 0.005$ for $N = 10\,000$ ($q_0^{tr} = 0.0498$) and to a higher value of $q_t^{tr} = 0.0083$ for 20 000 particles ($q_0^{tr} = 0.0658$).

A natural query, therefore, would be whether there exists a scaling factor for a trapped condensate which brings these phase boundaries for different numbers of condensate particles [Fig. 9(a)] to the same plot. The asymptote of unit slope indicates, if we scale the p' and q' with $q_t^{tr}(N)$, which is the q' value at $p' = 0$, where the transition happens for a particular N, then all these phase boundaries merge [Fig. 9(b)] and approximately follow $(q'/q_t^{tr})^2 - (p'/q_t^{tr})^2 = 1$, the equation of a hyperbola, similar to the homogeneous condensate.

To determine the dependence of the scaling factor q_t^{tr} on the number of condensate particles, we additionally estimated q_t^{tr} for $N = 7000$, 15 000, 30 000, 40 000, and 50 000 particles. Assuming a power-law dependence, from the log q_t^{tr} vs log N plot, we find that the scaling factor depends on the number of particles roughly as $q_t^{tr} \sim N^{3/4}$ [Fig. 10(a)].

Note that, in the absence of trapping, the PM-polar phase transition happens at a quadratic Zeeman term, $q_t^{\rm hom} = 2|c_1|n$ at $p = 0$. In that case, the number density is a constant. If we map the TF-approximated trapped condensate to the homogeneous counterpart by replacing the constant density with the TF-approximated average density, one can get to an estimation of the $q_t^{\rm TF}$.

The total number present in the condensate can be obtained by integrating the number density, which in the TF

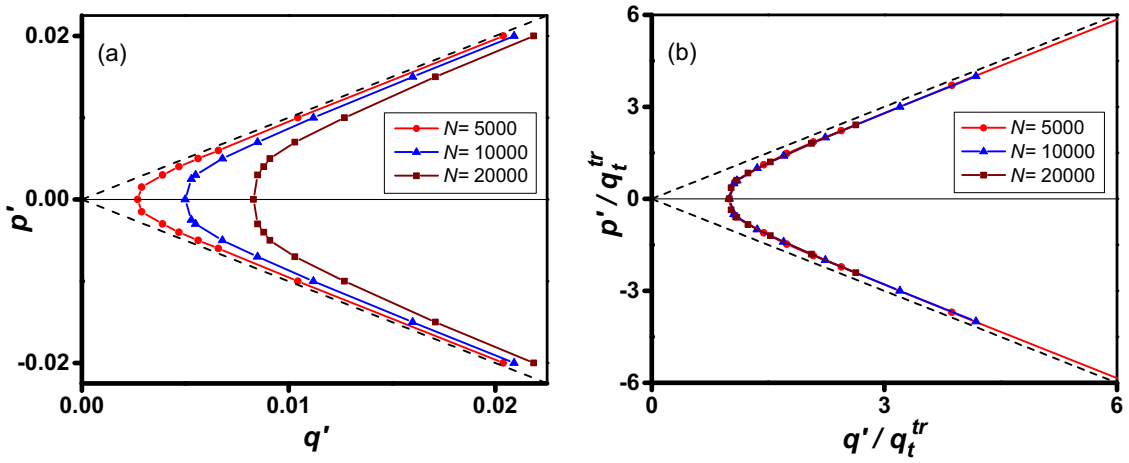

FIG. 9. (a) PM-polar phase transition boundary in q', p' parameter space under harmonic confinement for 5000, 10 000, and 20 000 condensate particles (in the red circle, blue triangle, and brown square markers). All the phase boundaries asymptotically follow the $|p'| = q'$ line for large values of p' and q', similar to the homogeneous condensate, while if we increase the number of particles, the range of q' at $p' = 0$ for which the PM state becomes the ground state increases. (b) The phase boundaries are plotted by scaling the quadratic and linear Zeeman terms with q_t^{tr}, where q_t^{tr} is the quadratic Zeeman strength for which the PM-polar transition happens at $p' = 0$ for a particular N. In these scaled coordinates, all the phase boundaries approximately follow the equation $(q'/q_t^{tr})^2 - (p'/q_t^{tr})^2 = 1$, the equation of a hyperbola, similar to the homogeneous condensates. All the quantities shown in this figure are dimensionless.

approximation

$$\int_0^R 4\pi\zeta^2\left[\mu'_{\rm TF} - \frac{1}{2}\zeta^2\right]d\zeta \sim N, \tag{41}$$

gives a relation between the TF radius R and the number of particles, N. As $\mu'_{\rm TF} = R^2/2$, the TF radius varies with N as $R \sim N^{1/5}$, which leads to the volume $V \sim R^3 \sim N^{3/5}$. So, the average density in the TF approximation depends on N as, $n_{\rm avg} = N/V \sim N^{2/5}$.

If we replace the constant density with the TF-approximated average density, one can estimate $q_t^{\rm TF} \sim N^{2/5}$, which is in contrast to the more accurate estimation obtained from the multimodal VM. On the other hand, the parameter q_0^{tr} depends on the number as $q_0^{tr} \sim N^{2/5}$. As a result, the ratio of these two parameters varies as $q_t^{tr}/q_0^{tr} \sim N^{7/20} \sim N^{0.35}$, which is verified from the slope of the $\log_{10}(q_t^{tr}/q_0^{tr})$ vs $\log_{10} N$ plot in Fig. 10(b).

For a condensate under 3D harmonic confinement, the VM estimates that $q_t^{tr} < q_0^{tr}$, which the numerical results also agree with (see Appendix C). In the particle number regime that we have considered, the ratio (q_t^{tr}/q_0^{tr}) is small but it increases when we increase the particle number [see inset in Fig. 10(b)]. This ratio gives an idea about the range of q' where although the PM state exists, it does not exist as a ground state $(q_t^{tr} < q' < q_0^{tr})$.

Now it can be physically understood why there is a significant shift in the phase boundary for a trapped situation compared to the homogeneous counterpart. For a

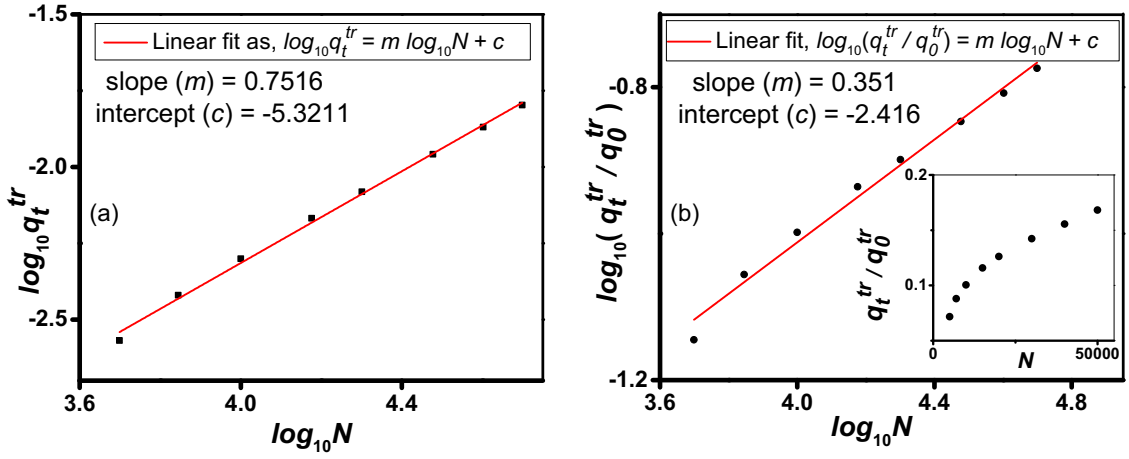

FIG. 10. (a) The scaling q_t^{tr} to vary with the number of particles as a power function $q_t^{tr} \propto N^m$. Using a linear fit, the slope of $\log q_t^{tr}$ vs $\log N$, which corresponds to the power m, is obtained, i.e., $m \approx 0.75$. This shows that the scaling factor q_t^{tr} varies approximately as $q_t^{tr} \propto N^{3/4}$ for 3D isotropic harmonic trapping. (b) The ratio q_t^{tr}/q_0^{tr} depends on N as a power law, $q_t^{tr}/q_0^{tr} \sim N^{0.35} \sim N^{7/20}$. As, $q_t^{tr} \sim N^{3/4}$, q_0^{tr} depends on N as $q_0^{tr} \sim N^{2/5}$. Inset: The ratio q_t^{tr}/q_0^{tr} increases with an increase in N.

homogeneous condensate, the energy (or the energy density) of the PM and polar states are compared by keeping the same constant density for these two states. However, in a trapped situation, the density varies over space. Even the average total density or the peak density is different for these two states. While the spin-spin interaction term (λ_1) appears in the subcomponent as well as the total density distribution for the PM state, the polar state density profile does not depend on λ_1. If we increase $|\lambda_1|$ (keeping p' and q' unchanged), the peak density of the PM state gets increased [as $\lambda_1 < 0$ and it comes in the density expression roughly as $u^{PM} \sim 1/(\lambda_0 + \lambda_1)$], while the polar state remains unaffected. For the trapped situation, one has to do the comparison for a fixed number of condensate particles, which is realistic as well. The mismatch in the density profile would contribute to a different potential energy, kinetic energy, and even a different spin-independent interaction energy ($\sim\lambda_0 \int d\zeta\, \zeta^2 u_{tot}^2$) for the PM state and the polar state. On the other hand, there would be a significant contribution of the tail part of the condensate in the kinetic energy, the potential energy caused by external trapping, and the interaction energy which is completely neglected in the TF approximation.

The strength of q', which causes the energy balance at the phase boundary, has to be estimated keeping all the energy contributions coming from the full condensate profile of both the states. This is exactly what the VM does, which results in an accurate total energy comparison of these two states to locate the phase boundary that cannot be trivially calculated by extrapolating the homogeneous results.

V. DISCUSSION

We have presented, in this paper, an accurate analytical description of the multicomponent ground states of a harmonically trapped spin-1 condensate. Even in the so-called TF regime, where the overall density of the condensate is high enough to supposedly neglect the kinetic energy contribution, the TF approximation can go wrong when applied to multicomponent states. On the other hand, the SMA can, as well, be significantly inaccurate in handling such multicomponent situations. This requires a general multimodal treatment taking into consideration the kinetic energy term, which the VM provides. The VM correctly captures multicomponent ground states because it can accurately estimate trapped density profiles even in the low-density regions. These tail parts of low densities are where the kinetic energy contribution is more significant than the interaction energy.

Moreover, the VM can be easily implemented for 3D harmonic trapping, where doing numerical simulation is well known to be computationally expensive. Utilizing this advantage, we further explored the phase boundary between the phase-matched and the polar state under isotropic harmonic trapping. We have presented a detailed analysis of the shift of the phase boundary in the trapped case, which numerical results also support. Despite the significant shift, these boundaries bear clear qualitative correspondence with the homogeneous case. The scaling of these phase boundaries with the particle number of trapped condensates is found out. This scaling deviates significantly from that estimated from a TF-approximated trapped case equivalent to the homogeneous case.

The data sets generated and analyzed during the current study are available from the corresponding author at a reasonable request.

ACKNOWLEDGMENTS

P.K.K. would like to thank the Council of Scientific and Industrial Research (CSIR), India, for providing funding during this research. The support and the resources provided by PARAM Brahma Facility under the National Supercomputing Mission, Government of India, at the Indian Institute of Science Education and Research, Pune, are gratefully acknowledged. The support in the form of a research fellowship provided by I-HUB Quantum Technology Foundation, Pune, India, is acknowledged. We would like to thank the anonymous referees for their valuable suggestions which improved this article in many ways.

APPENDIX A: VARIATIONAL METHOD

To work with the nonzero contribution of p and q, we extend the variational method introduced in Ref. [56]. First, we will present the general method in a brief manner and then we will implement that for the PM state and the AFM state, which are the multicomponent states of interest to this article.

To implement the variational method, in the presence of quasi-one-dimensional harmonic trapping, one needs to solve the GP equations [Eqs. (13) and (14)] by getting rid of the kinetic energy terms which will yield the subcomponent densities in the high-density region near the center of the trap, where the kinetic energy can be neglected in comparison to the interaction terms. The subcomponent densities will get a functional form specific to different stationary states. Next, we assume that, near the low-density region where the kinetic energy is of relevance and the interaction terms are very small, the mean fields can be described in terms of the first few lowest harmonic oscillator states. Thus the density distributions can be written as

$$u_{\pm1,0}^{\text{in}} = g_{\pm1,0}(\mu', \zeta) \quad \text{for} \quad |\zeta| \leqslant \zeta_{\pm1,0}^{\text{mat}}, \tag{A1}$$

$$u_{\pm1,0}^{\text{out}} = (a_{\pm1,0} + c_{\pm1,0}|\zeta| + d_{\pm1,0}\zeta^2)\exp\left(-\frac{\zeta^2}{b_{\pm1,0}}\right) \quad \text{for} \quad |\zeta| \geqslant \zeta_{\pm1,0}^{\text{mat}}, \tag{A2}$$

where $u_{\pm1,0}^{\text{in(out)}}$ are the subcomponent densities in the high-density (low-density) region. Now we impose the condition that for each subcomponent the low-density $\sqrt{u_{\pm1,0}^{\text{out}}}$ and the high-density $\sqrt{u_{\pm1,0}^{\text{in}}}$ expressions match at a point ζ^{mat}. Not only do they match but their first three derivatives also match. These four constraints provide the four unknowns a, b, c, and d for each subcomponent in terms of the matching points and the parameter μ'. Note that imposing the matching condition up to three derivatives also gives a smooth profile of the corresponding kinetic energy.

Once all the coefficients in Eq. (A2) are known, the subcomponent density profile only depends on the parameter μ'

and the matching points. The parameter μ' can be obtained as a function of the matching points from

$$\sum_{m=-1}^{1}\left[\int_0^{\zeta_m^{\rm mat}} u_m^{\rm in}(\mu',\zeta)d\zeta+\int_{\zeta_m^{\rm mat}}^{\infty} u_m^{\rm out}\big(\mu',\zeta,\zeta_m^{\rm mat}\big)d\zeta\right]=N, \tag{A3}$$

where N is the total number of condensate particles. Note that one might expect that the right side should be $N/2$ as the integration is running in only one direction from the center of the trap, but it is N in the right side due to Eqs. (11) and (12), which we used to write the GP equation in nondimensional form. From Eq. (A3) the parameter μ' can be written as a function of the matching points for a particular N.

Thus the subcomponent number densities and hence the total energy of a stationary state [Eq. (10)] also become the function of the matching points only. From the minimization of the total energy in the parameter space of the matching points, one can determine the matching points as well as the total energy.

1. Variational method for the PM state

For the PM state, all the subcomponents are populated followed by the phase-matching condition, i.e., the relative phase being $\theta_r=0$. One can solve the phase stationary equations [Eqs. (13) and (14)] by ignoring the kinetic part to get the functional form of the subcomponent densities $g_{\pm1,0}(\mu',\zeta)$ in the high-density region as

$$u_m^{\rm in}=k_m\left[\frac{\mu'_m-\zeta^2/2}{\lambda_0+\lambda_1}\right], \tag{A4}$$

where

$$k_1=\frac{(p'+q')^2}{4q'^2},\quad k_0=\frac{q'^2-p'^2}{2q'^2},\quad k_{-1}=\frac{(p'-q')^2}{4q'^2}, \tag{A5}$$

and

$$\begin{aligned}\mu'_{\pm1}&=\mu'_{\rm eff}+(\lambda_0+\lambda_1)\frac{q'^2-p'^2}{2\lambda_1 q'},\\ \mu'_0&=\mu'_{\rm eff}-(\lambda_0+\lambda_1)\frac{q'^2+p'^2}{2\lambda_1 q'},\\ \mu'_{\rm eff}&=\mu'+\frac{p'^2-q'^2}{2q'}.\end{aligned} \tag{A6}$$

Applying the four matching conditions mentioned earlier, the unknown coefficients in the low-density expression for each subcomponent can be obtained as

$$\begin{aligned}a_m=&\frac{1}{-8\mu'_m+4\zeta_m^2}\big(\mu'_m\big(-56\mu'_m+70\zeta_m^2+4\kappa_m\big)\\&-3\zeta_m^2\big(14\zeta_m^2+\kappa_m-6\mu'_m\big)\big)\exp\left(\frac{12\zeta_m^2}{\kappa_m}\right),\end{aligned} \tag{A7}$$

$$b_m=\frac{\kappa_m}{12}, \tag{A8}$$

$$c_m=\frac{48\zeta_m^3\big(-12\mu'_m+6\zeta_m^2+\kappa_m\big)}{\kappa_m^2}\exp\left(\frac{12\zeta_m^2}{\kappa_m}\right), \tag{A9}$$

$$\begin{aligned}d_m=&\frac{1}{2\zeta_m^2\big(-2\mu'_m+\zeta_m^2\big)}\Big(-\zeta_m^2\big(\kappa_m+13\zeta_m^2-6\mu'_m\big)\\&-12(\mu'_m)^2+\mu'_m\big(14\zeta_m^2+\kappa_m\big)\Big)\exp\left(\frac{12\zeta_m^2}{\kappa_m}\right),\end{aligned} \tag{A10}$$

where ζ_m is an abbreviation for the matching point $\zeta_m^{\rm mat}$ and

$$\kappa_m=6\mu'_m-9\zeta_m^2+\sqrt{36(\mu'_m)^2-12\mu'_m\zeta_m^2+33\zeta_m^4}, \tag{A11}$$

given the subcomponent densities in the low-density region are represented as

$$u_m^{\rm out}=\frac{k_m}{\lambda_0+\lambda_1}(a_m+c_m|\zeta|+d_m\zeta^2)\exp\left(-\frac{\zeta^2}{b_m}\right). \tag{A12}$$

Now applying Eq. (A3) one can find the parameter μ' [see the $\mu'_{\rm eff}$ expression in Eq. (A6)] for different values of ζ_m. Note that, as $\mu'_1=\mu'_{-1}$ [see Eq. (A6)], the matching points are the same for these two components, i.e., $\zeta_1^{\rm mat}=\zeta_{-1}^{\rm mat}$. The total energy [Eq. (10)] for the PM state becomes only a function of the matching points.

From a physical perspective, the high-density expressions of u_0 and $u_{\pm1}$ were found by getting rid of the kinetic terms in Eqs. (13) and (14). So the high-density expressions given in Eq. (A4) are true as long as all the subcomponents are in the high-density region. If we focus on the case presented in the article, for $p'=0.01$ and $q'=0.3$, near the TF radius the $u_{\pm1}$ subcomponent does not follow the high-density expressions. As a result, one can neglect the derivative term in Eq. (13) but cannot neglect the same in Eq. (14). This precisely makes the multicomponent stationary states beyond the reach of the TF approximation as long as the subcomponents do not follow the same spatial distribution.

Precisely for the reason stated above, one has to shift the focus toward the total density. So, instead of using the high-density expression $u_0^{\rm in}$ we will use the total density expression,

$$u_{tot}^{\rm in}=k_{tot}\left[\frac{\mu'_{\rm eff}-\zeta^2/2}{\lambda_0+\lambda_1}\right], \tag{A13}$$

written in the same fashion as Eq. (A4), where $k_{tot}=1$. Now instead of the $m=0$ component, the same expressions [Eqs. (A7)–(A10)] would also provide the total density expression in the low-density region [$u_{tot}^{\rm out}$ in Eq. (A12)]. The u_0 component can be found by subtracting the other two component densities from the total density.

Thus, the total energy of the PM state only becomes a function of the two matching points, $\zeta_{tot}^{\rm mat}$ and $\zeta_{\pm1}^{\rm mat}$. Minimizing the total energy with respect to these two parameter variations one can get the matching points and the total energy itself. And as the matching points are found, the analytical density expressions are also obtained.

Note that the spin-spin interaction strength (λ_1) is responsible for the subcomponent density distribution. For

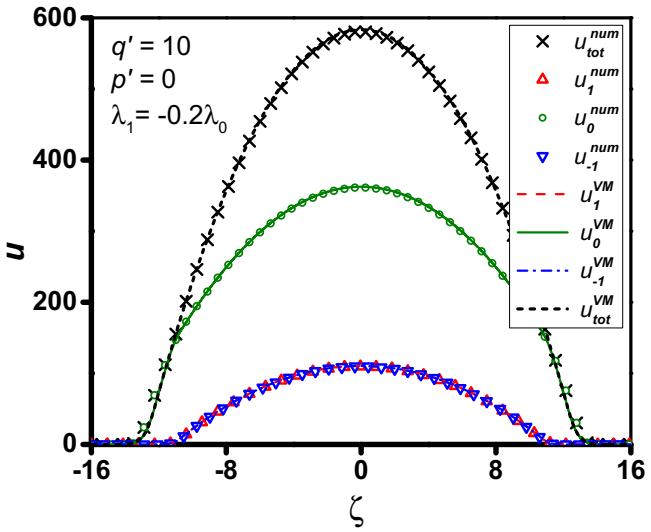

FIG. 11. Number density profile of the PM state in quasi-one-dimensional harmonic confinement with $p' = 0$, $q' = 10$, $\lambda_0 = 17.66 \times 10^{-2}$, and $\lambda_1 = -0.2 \times 17.66 \times 10^{-2}$. The subcomponent densities u_0, u_1, and u_{-1} obtained from the variational method (lines) and numerical simulation (markers) are in agreement even if the spin-dependent and spin-independent interaction coefficients are of comparable strengths. The total density profiles (numerical in black squares and VM profile in black dashed lines) are also in agreement.

^{87}Rb, the ratio of the spin-interaction coefficient with the spin-independent interaction strength is very small ($|\lambda_1|/\lambda_0 \sim 1/300$). The accuracy of the variational method does not depend on this ratio being small; rather it works perfectly even when spin-spin and spin-independent interactions are of comparable strength (Fig. 11).

2. Variational method for the AFM state

When the u_1 and the u_{-1} components are populated (even though they are unequally populated for nonzero values of p'; see Table I) the stationary state is referred to as the antiferromagnetic or, in short, AFM state. When both the subcomponents are in the high-density regions, one can write the densities by neglecting the derivative terms in the phase equations as

$$u_{\pm1}^{\rm in} = k_{\pm1}\left[\frac{\mu'_{\pm1} - \zeta^2/2}{\lambda_0}\right], \tag{A14}$$

where $k_{\pm1} = 1/2$ and

$$\mu'_{\pm1} = \mu' - q' \pm \frac{\lambda_0}{\lambda_1}p'. \tag{A15}$$

The subcomponent density u_0 is zero throughout.

Note that the high-energy expressions are valid as long as the subcomponent density is high enough so that the derivative terms can be safely ignored. But for $p' = 0.2$ and $q' = -0.5$ (the case we discussed), the u_{-1} component has a lesser TF radius than the other component. As a result of it near the TF radius of the u_{-1} component, the high-density expression of the u_1 component would be invalid, for the reasons stated earlier. So, we will take the total density and the u_{-1} component to implement the variational method.

In the high-density region, the total density can be written as

$$u_{tot}^{\rm in} = k_{tot}\left[\frac{\mu'_{tot} - \zeta^2/2}{\lambda_0}\right], \tag{A16}$$

where $k_{tot} = 1$. Now one can write the low-density expressions as

$$u_m^{\rm out} = \frac{k_m}{\lambda_0}(a_m + c_m|\zeta| + d_m\zeta^2)\exp\left(-\frac{\zeta^2}{b_m}\right), \tag{A17}$$

where $u_{-1}^{\rm out}$, and $u_{tot}^{\rm out}$ represents the $m = -1$ subcomponent and the total density in the low-density region of the trap. The coefficients will have the same expressions as Eqs. (A7)–(A11). Following the same method as explained earlier one can minimize the total energy corresponding to this stationary state in the parameter space of the matching points $\zeta_{tot}^{\rm mat}$ and $\zeta_{-1}^{\rm mat}$ which provides the analytical form of the full profile of the condensate in terms of the total density and the u_{-1} component. By subtracting the u_{-1} component from the total density profile one can get to the u_1 component.

APPENDIX B: VARIATIONAL METHOD IN 3D ISOTROPIC HARMONIC CONFINEMENT

If we consider a condensate trapped inside an isotropic 3D harmonic confinement with trapping frequency ω, one can write the GP equation in a nondimensional form using Eqs. (38) and (39),

$$\left\{-\frac{1}{2}\frac{1}{\zeta^2}\frac{d}{d\zeta}(\zeta^2\frac{d}{d\zeta}) + \frac{1}{2}\zeta^2 + \lambda_0 u - \mu' + \lambda_1\left(u_1 + u_{-1} + 2\sqrt{u_{-1}u_1}\cos\theta_r\right)\right\}\sqrt{u_0} = 0, \tag{B1}$$

$$\left\{-\frac{1}{2}\frac{1}{\zeta^2}\frac{d}{d\zeta}(\zeta^2\frac{d}{d\zeta}) + \frac{1}{2}\zeta^2 + \lambda_0 u - \mu' \pm \lambda_1(u_1 - u_{-1}) \mp p' + q'\right\}\sqrt{u_{\pm1}} + \lambda_1 u_0(\sqrt{u_{\pm1}} + \sqrt{u_{\mp1}}\cos\theta_r) = 0, \tag{B2}$$

where, due to isotropy, we have only considered the radial part of the Laplacian in the spherical polar coordinate.

Similar to the 1D situation one can estimate the high-density expressions by neglecting the Laplacian term for a stationary state, followed by the assumption in Eq. (A12) serving as the number density profile in the low-density region. Here, ζ is the radial distance from the center of the trap. The unknown parameters in Eq. (A12) for the PM state under 3D harmonic confinement assume the same expressions given in Eqs. (A7)–(A10).

The only difference with the 1D situation is in the form of the relation that is used to estimate the parameter μ'. Integrating the subcomponent densities would provide the total number of condensate particles, which in the nondimensional form can be written as [following the scaling in

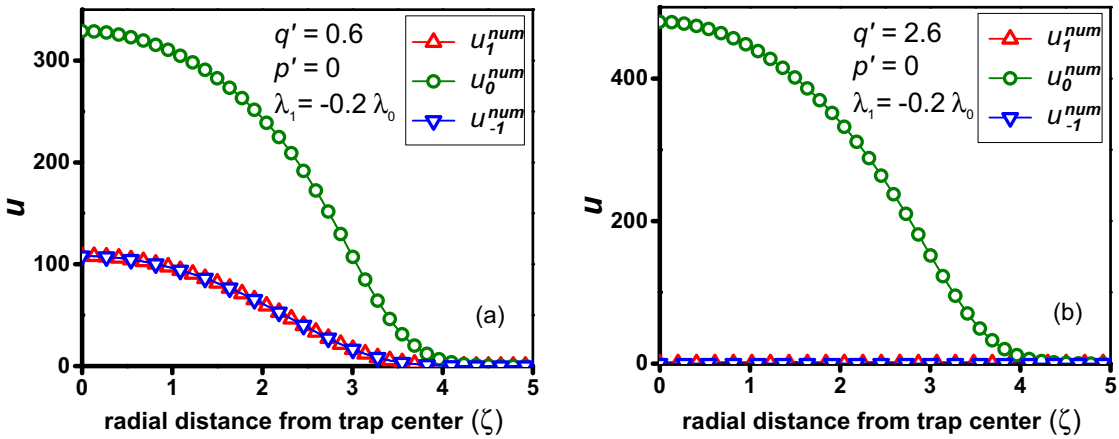

FIG. 12. Numerical profiles for u_0 (shown in green circles), u_1 (red triangles) and u_{-1} (blue inverted triangles) at $\lambda_0 = 1.484 \times 10^{-2}$ and $\lambda_1 = -0.2 \times 1.484 \times 10^{-2}$. Starting with the same initial condition at $p' = 0$, (a) the PM state becomes the ground state at $q' = 0.6$ and (b) the polar state is selected as the ground state at $q' = 2.6$. These numerical results verify the VM estimation that the PM-polar phase boundary is at $q_t^{tr} < q_0^{tr}$ (as $q_0^{tr} \approx 3.28$). All the quantities shown in this figure are dimensionless.

Eqs. (38) and (39)]

$$\sum_{m=-1}^{1}\left[\int_0^{\zeta_m^{\rm mat}} u_m^{\rm in}(\mu',\zeta)\zeta^2 d\zeta + \int_{\zeta_m^{\rm mat}}^{\infty} u_m^{\rm out}\left(\mu',\zeta,\zeta_m^{\rm mat}\right)\zeta^2 d\zeta\right] = \frac{N}{3}. \tag{B3}$$

From this equation, one can estimate μ' for the matching points $\zeta_m^{\rm mat}$ for a condensate with N particles. And following the procedure of minimization of the total energy, the matching points are obtained.

For the polar state, the implementation of the variational method is straightforward. Only the u_0 component is populated for the polar state; hence Eq. (B1) becomes trivial. The number density expression in the high-density region for this state can be obtained by neglecting the Laplacian term in Eq. (B2):

$$u_0^{\rm in}|_{\rm polar} = \frac{\mu' - \frac{1}{2}\zeta^2}{\lambda_0}. \tag{B4}$$

The number density in the low-density region would follow,

$$u_0^{\rm out}|_{\rm polar} = \frac{1}{\lambda_0}(a_0 + c_0\zeta + d_0\zeta^2)\exp\left(-\frac{\zeta^2}{b_0}\right), \tag{B5}$$

where the coefficients a_0, b_0, c_0, and d_0 follow the same expressions as Eqs. (A7)–(A10).

For the polar state, only one component being present makes the variational method even easier to implement. Following the same method discussed earlier, one has to estimate the matching point $\zeta_0^{\rm mat}$ by minimizing the total energy in the one-dimensional parameter space of $\zeta_0^{\rm mat}$. Note that the total energy of the polar state does not depend on the linear and quadratic Zeeman terms.

APPENDIX C: NUMERICAL RESULTS IN 3D ISOTROPIC HARMONIC CONFINEMENT

In Sec. IV, using the variational method we estimated the phase boundary for an isotropic 3D harmonic trapping. At $p = 0$, it is shown that the phase transition happens at $q' = q_t^{tr}$, whereas the PM state ceases to exist at q_0^{tr}, with $q_t^{tr} < q_0^{tr}$.

We used the imaginary time propagation method (split-step Fourier method [71]) as a numerical scheme to get to the ground state. In this scheme, in the presence of competing ground-state candidates with very closely separated energy, it takes a very large number of steps to converge to a solution. In close proximity of the phase boundary, this problem would arise, and exactly at the phase boundary one of the degenerate states would be favored depending on the initial condition after an extremely long time evolution. On top of that, the numerical value of the spin-spin interaction term (λ_1) that we considered is very small. As λ_1 causes the spin-exchange interaction [71], starting with an arbitrary initial condition it takes a very long time to converge to the ground state even when the simulation is done avoiding the proximity of the phase boundary.

To get rid of this limitation, we did the numerical simulation, for the same $\lambda_0 = 17.66 \times 10^{-2}$ but increasing the strength of λ_1 to $\lambda_1 = -0.2 \times \lambda_0$, which resulted in much faster convergence to the ground state. For this value of λ_1 at $N = 10\,000$, the VM suggests that the phase transition at $p' = 0$ happens at $q_t^{tr} \approx 1.6$, while $q_0^{tr} \approx 3.28$ (for $q' > q_0^{tr}$, the PM state does not exist). So, in the region $q_t^{tr} < q' < q_0^{tr}$, according to the VM, the PM state, although it exists, is not favored as the ground state.

Avoiding the close proximity of the VM estimated phase boundary (for the previously mentioned reason), we did numerical simulation at $q' = 0.6$ ($< q_t^{tr}$), and $q' = 2.6$ ($> q_t^{tr}$) starting with the same initial condition of $u_0^{\rm ini} = 600\,\exp(-0.18\,\zeta^2)$, $u_{\pm1}^{\rm ini} = 10\,\exp(-0.18\,\zeta^2)$. The numerical results shown in Fig. 12(a) verify that the PM state is the ground state (at $q' < q_t^{tr}$).

On the other hand, at $q' = 2.6$ (which is in the region $q_t^{tr} < q' < q_0^{tr}$), the polar state emerges as the ground state [Fig. 12(b)]. This numerical result verifies the VM estimation of the phase transition to happen at $q_t^{tr} < q_0^{tr}$. Note that, at $q' = 2.6$, although the PM state exists with the peak density of $u_{\pm1}(\zeta = 0) \approx 26$, the numerical result clearly shows it is not selected as the ground state.

[1] K. B. Davis, M. O. Mewes, M. R. Andrews, N. J. van Druten, D. S. Durfee, D. M. Kurn, and W. Ketterle, Phys. Rev. Lett. **75**, 3969 (1995).

[2] M. H. Anderson, J. R. Ensher, M. R. Matthews, C. E. Wieman, and E. A. Cornell, Science **269**, 198 (1995).

[3] C. C. Bradley, C. A. Sackett, J. J. Tollett, and R. G. Hulet, Phys. Rev. Lett. **75**, 1687 (1995).

[4] S. Giorgini, L. P. Pitaevskii, and S. Stringari, Phys. Rev. A **54**, R4633(R) (1996).

[5] F. Dalfovo and S. Stringari, Phys. Rev. A **53**, 2477 (1996).

[6] S. Stringari, Phys. Rev. Lett. **77**, 2360 (1996).

[7] N. Dupont, G. Chatelain, L. Gabardos, M. Arnal, J. Billy, B. Peaudecerf, D. Sugny, and D. Guéry-Odelin, PRX Quantum **2**, 040303 (2021).

[8] R. Senaratne, S. V. Rajagopal, T. Shimasaki, P. E. Dotti, K. M. Fujiwara, K. Singh, Z. A. Geiger, and D. M. Weld, Nat. Commun. **9**, 2065 (2018).

[9] Y. Yamamoto and Y. Takahashi, Bose-Einstein condensation: A platform for quantum simulation experiments, in *Principles and Methods of Quantum Information Technologies*, edited by Y. Yamamoto and K. Semba (Springer Japan, Tokyo, 2016), pp. 265–307

[10] T. Bravo, C. Sabín, and I. Fuentes, EPJ Quantum Technol. **2**, 3 (2015).

[11] J. I. Cirac and P. Zoller, Nat. Phys. **8**, 264 (2012).

[12] I. M. Georgescu, S. Ashhab, and F. Nori, Rev. Mod. Phys. **86**, 153 (2014).

[13] D. Becker, M. D. Lachmann, S. T. Seidel, H. Ahlers, A. N. Dinkelaker, J. Grosse, O. Hellmig, H. Müntinga, V. Schkolnik, T. Wendrich, A. Wenzlawski, B. Weps, R. Corgier, T. Franz, N. Gaaloul, W. Herr, D. Lüdtke, M. Popp, S. Amri, H. Duncker *et al.*, Nature (London) **562**, 391 (2018).

[14] S. S. Szigeti, S. P. Nolan, J. D. Close, and S. A. Haine, Phys. Rev. Lett. **125**, 100402 (2020).

[15] S. Gupta, K. Dieckmann, Z. Hadzibabic, and D. E. Pritchard, Phys. Rev. Lett. **89**, 140401 (2002).

[16] A. O. Jamison, J. N. Kutz, and S. Gupta, Phys. Rev. A **84**, 043643 (2011).

[17] D. Hanneke, S. Fogwell, and G. Gabrielse, Phys. Rev. Lett. **100**, 120801 (2008).

[18] P. Dutta, S. S. Maurya, K. Patel, K. Biswas, J. Mangaonkar, S. Sarkar, and U. D. Rapol, J. Indian Inst. Sci. **103**, 609 (2023).

[19] J. R. Ensher, D. S. Jin, M. R. Matthews, C. E. Wieman, and E. A. Cornell, Phys. Rev. Lett. **77**, 4984 (1996).

[20] W. Ketterle, M. R. Andrews, K. B. Davis, D. S. Durfee, D. M. Kurn, M. O. Mewes, and N. J. van Druten, Phys. Scr. **1996**, 31 (1996).

[21] D. M. Stamper-Kurn, M. R. Andrews, A. P. Chikkatur, S. Inouye, H.-J. Miesner, J. Stenger, and W. Ketterle, Phys. Rev. Lett. **80**, 2027 (1998).

[22] M.-S. Chang, C. D. Hamley, M. D. Barrett, J. A. Sauer, K. M. Fortier, W. Zhang, L. You, and M. S. Chapman, Phys. Rev. Lett. **92**, 140403 (2004).

[23] D. M. Stamper-Kurn and W. Ketterle, in *Les Houches - Ecole d'Ete de Physique Theorique* (Springer, Berlin, 2001), pp. 139–217.

[24] Y. Kawaguchi, H. Saito, and M. Ueda, Phys. Rev. Lett. **97**, 130404 (2006).

[25] A. E. Leanhardt, Y. Shin, D. Kielpinski, D. E. Pritchard, and W. Ketterle, Phys. Rev. Lett. **90**, 140403 (2003).

[26] E. Timmermans, Phys. Rev. Lett. **81**, 5718 (1998).

[27] T. Świsłocki and M. Matuszewski, Phys. Rev. A **85**, 023601 (2012).

[28] K.-T. Xi, J. Li, and D.-N. Shi, Phys. Rev. A **84**, 013619 (2011).

[29] S. Bandyopadhyay, A. Roy, and D. Angom, Phys. Rev. A **96**, 043603 (2017).

[30] T. Isoshima, K. Machida, and T. Ohmi, Phys. Rev. A **60**, 4857 (1999).

[31] M. Matuszewski, T. J. Alexander, and Y. S. Kivshar, Phys. Rev. A **78**, 023632 (2008).

[32] M. Matuszewski, T. J. Alexander, and Y. S. Kivshar, Phys. Rev. A **80**, 023602 (2009).

[33] T.-L. Ho and V. B. Shenoy, Phys. Rev. Lett. **77**, 3276 (1996).

[34] S. Bhuvaneswari, K. Nithyanandan, and P. Muruganandam, J. Phys. Commun. **2**, 025008 (2018).

[35] L. Wen, W. M. Liu, Y. Cai, J. M. Zhang, and J. Hu, Phys. Rev. A **85**, 043602 (2012).

[36] Z. Liu, J. Math. Phys. **50**, 102104 (2009).

[37] L. Zhu and J. Li, Mod. Phys. Lett. B **31**, 1750215 (2017).

[38] S. Tojo, Y. Taguchi, Y. Masuyama, T. Hayashi, H. Saito, and T. Hirano, Phys. Rev. A **82**, 033609 (2010).

[39] J. Li, Y.-M. Yu, K.-J. Jiang, and W.-M. Liu, arXiv:1802.00138.

[40] K. L. Lee, N. B. Jørgensen, I.-K. Liu, L. Wacker, J. J. Arlt, and N. P. Proukakis, Phys. Rev. A **94**, 013602 (2016).

[41] J. Sabbatini, W. H. Zurek, and M. J. Davis, Phys. Rev. Lett. **107**, 230402 (2011).

[42] S. Gautam and S. K. Adhikari, Phys. Rev. A **90**, 043619 (2014).

[43] S. Gautam and D. Angom, J. Phys. B: At. Mol. Opt. Phys. **44**, 025302 (2011).

[44] H. Saito and M. Ueda, Phys. Rev. A **72**, 023610 (2005).

[45] P. K. Kanjilal and A. Bhattacharyay, Phys. Scr. **95**, 045702 (2020); **97**, 129501 (2022).

[46] M. Ueda, Rep. Prog. Phys. **77**, 122401 (2014).

[47] H. E. Nistazakis, D. J. Frantzeskakis, P. G. Kevrekidis, B. A. Malomed, and R. Carretero-González, Phys. Rev. A **77**, 033612 (2008).

[48] T. M. Bersano, V. Gokhroo, M. A. Khamehchi, J. D'Ambroise, D. J. Frantzeskakis, P. Engels, and P. G. Kevrekidis, Phys. Rev. Lett. **120**, 063202 (2018).

[49] G. C. Katsimiga, S. I. Mistakidis, P. Schmelcher, and P. G. Kevrekidis, New J. Phys. **23**, 013015 (2021).

[50] G. Hegde, S. M. Jose, and R. Nath, Phys. Rev. A **106**, 043307 (2022).

[51] S. I. Mistakidis, A. G. Volosniev, R. E. Barfknecht, T. Fogarty, T. Busch, A. Foerster, P. Schmelcher, and N. T. Zinner, Phys. Rep. **1042**, 1 (2023).

[52] T.-L. Ho, Phys. Rev. Lett. **81**, 742 (1998).

[53] S. Yi, O. E. Müstecaplıoğlu, C. P. Sun, and L. You, Phys. Rev. A **66**, 011601 (2002).

[54] W. Zhang, S. Yi, and L. You, New J. Phys. **5**, 77 (2003).

[55] S. Gautam and S. K. Adhikari, Phys. Rev. A **92**, 023616 (2015).

[56] P. K. Kanjilal and A. Bhattacharyay, Eur. Phys. J. Plus **137**, 547 (2022).

[57] N. T. Phuc, Y. Kawaguchi, and M. Ueda, Phys. Rev. A **84**, 043645 (2011).

[58] Y. Kawaguchi, N. T. Phuc, and P. B. Blakie, Phys. Rev. A **85**, 053611 (2012).

[59] E. Serrano-Ensástiga and F. Mireles, Phys. Lett. A **492**, 129188 (2023).

[60] K. M. Mittal, S. I. Mistakidis, P. G. Kevrekidis, and P. Schmelcher, Phys. Rev. A **102**, 013302 (2020).
[61] J. Stenger, S. Inouye, D. Stamper-Kurn, H.-J. Miesner, A. Chikkatur, and W. Ketterle, Nature (London) **396**, 345 (1998).
[62] Y. Kawaguchi and M. Ueda, Phys. Rep. **520**, 253 (2012), spinor Bose-Einstein condensates.
[63] W. Zhang, D. L. Zhou, M.-S. Chang, M. S. Chapman, and L. You, Phys. Rev. A **72**, 013602 (2005).
[64] J. Jie, Q. Guan, S. Zhong, A. Schwettmann, and D. Blume, Phys. Rev. A **102**, 023324 (2020).
[65] J. Jie, S. Zhong, Q. Zhang, I. Morgenstern, H. G. Ooi, Q. Guan, A. Bhagat, D. Nematollahi, A. Schwettmann, and D. Blume, Phys. Rev. A **107**, 053309 (2023).
[66] S. Ganesh, Master's thesis, KTH Royal Institute of Technology, 2019.
[67] L. E. Sadler, J. M. Higbie, S. R. Leslie, M. Vengalattore, and D. M. Stamper-Kurn, Nature (London) **443**, 312 (2006).
[68] H. Saito, Y. Kawaguchi, and M. Ueda, Phys. Rev. A **75**, 013621 (2007).
[69] H. Saito, Y. Kawaguchi, and M. Ueda, Phys. Rev. A **76**, 043613 (2007).
[70] T. Ohmi and K. Machida, J. Phys. Soc. Jpn. **67**, 1822 (1998).
[71] P. Kaur, A. Roy, and S. Gautam, Comput. Phys. Commun. **259**, 107671 (2021).
[72] D. J. Papoular, G. V. Shlyapnikov, and J. Dalibard, Phys. Rev. A **81**, 041603(R) (2010).